

Biomedical Applications of
NMR Imaging and Diffusion Studies
Using Thermal And Hyperpolarized Xenon

by

Sameer Anil Sheth

Submitted to the Department of Physics
in partial fulfillment of the requirements for the degree of

Bachelor of Arts

at

HARVARD UNIVERSITY

May 11, 1998

© S. Sheth, 1998. All rights reserved.

The author hereby grants to Harvard University permission to reproduce
and to distribute copies of this thesis document
in whole or in part.

Author

Department of Physics
May 11, 1998

Certified by

Ronald Walsworth
Physicist
Thesis Advisor

Certified by

Costas Papaliolios
Professor of Physics
Thesis Supervisor

Certified by

Robert Westervelt
Professor of Physics
Thesis Reader

Accepted by

David Nelson
Chairman, Department of Physics

Biomedical Applications of
NMR Imaging and Diffusion Studies
Using Thermal And Hyperpolarized Xenon

by

Sameer Anil Sheth

Submitted to the Department of Physics

in partial fulfillment of the requirements for the degree of

Bachelor of Arts

at

HARVARD UNIVERSITY

May 11, 1998

ABSTRACT

We present results of NMR experiments performed on both thermal xenon and xenon hyperpolarized by spin exchange optical pumping. We have developed and characterized a self-contained apparatus mounted on a hand-cart which produces 644 ml of Xe hyperpolarized to approximately 1%. The measured relaxation rates in the cart manifold and detachable inhalation bag were large compared to gas residence time in these compartments. Our successful generation of a magnetic resonance (MR) image of laser polarized Xe in the inhalation bag leads us to believe that an MR image of polarized Xe inhaled in a human lung will be possible in the near future.

We also studied free and restricted diffusion of Xe gas, and found that our NMR pulse sequences for measuring diffusion were robust and produced results consistent with previously published data. The ability to measure restricted diffusion in human lung alveoli (~ 100 μm diameter) would provide valuable information about lung microstructure, including the surface area to volume ratio and porosity of alveoli. Towards this end, we experimented with the buffer gas sulfur hexafluoride (SF_6), hoping that it would decrease Xe diffusivity enough to allow the study of such small pores. We found that not only did SF_6 not significantly reduce Xe diffusivity, it also undesirably decreased T_2 . In addition, we began Xe NMR experiments in rat lung and report rough T_1 and T_2 estimates of 1 second and 2.1 msec, respectively.

Keywords: Magnetic resonance imaging; Magnetic resonance spectroscopy; Hyperpolarized noble gas; Hyperpolarized ^{129}Xe MRI; PGSE technique; Gas diffusion; Restricted diffusion; Porous media.

TABLE OF CONTENTS

I Introduction.....	1
II Theory	4
II.1 Nuclear Magnetic Resonance	4
II.2 Magnetic Resonance Imaging	12
II.3 Spin-exchange Optical Pumping	14
II.4 Free Diffusion	17
II.5 Restricted Diffusion	23
III Methods	26
III.1 Human Inhalation Cart	26
III.2 Diffusion Measurements	33
IV Results and Discussion	40
IV.1 Large-scale Polarization of Xe for Human MRI	40
IV.2 Diffusion Results	46
IV.2.1 Studies of thermal Xe free diffusion	46
IV.2.2 Studies of thermal Xe restricted diffusion	47
IV.2.3 Studies of laser polarized Xe free diffusion	49
IV.2.4 Studies of thermal Xe free diffusion in the presence of SF ₆	49
IV.2.5 Studies of diffusion in rat lung	51
V Conclusion	54
References	55
Acknowledgements	58

LIST OF FIGURES

II.1	T ₂ relaxation mechanism	7
II.2	Inversion-recovery method for measuring T ₁	9
II.3	CPMG method for measuring T ₂	10
II.4	Basic MR imaging sequence	14
II.5	Octadecyltrichlorosilane (OTS)	17
II.6	Pulsed gradient spin echo (PGSE) sequence	19
II.7	Pulsed gradient simulated echo (PGSTE) sequence	20
II.8	Bipolar PGSTE with n = 2	22
III.1	Front of human inhalation cart	27
III.2	Back of human inhalation cart	28
III.3	Freeze cell and manifold of human inhalation cart	29
III.4	Imaging sequence with low-angle pulse and gradient echo	33
III.5	Pulsed gradient echo (PGE)	37
III.6	Multiple pulsed gradient spin echo (MPGSE)	37
IV.1	Typical pump-up curve	40
IV.2	Typical T ₁ for pump cell	42
IV.3	Typical T ₁ for freeze cell	43
IV.4	Typical T ₁ for inhalation bag	44
IV.5	Image of inhalation bag	45
IV.6	Time-dependent (restricted) diffusion curve for 4 and 2 mm beads	48

LIST OF TABLES

IV.1	Effect of SF ₆ on Xe diffusivity	50
IV.2	Characterization of rat experiment test gas mixture	51
IV.3	Xe resonance in rat lung	51

I INTRODUCTION

The advent of Nuclear Magnetic Resonance (NMR) in the early 1950s allowed scientists to probe structure at an atomic level. Edward Purcell, one of the discoverers of NMR, alluded to its potentially vast ramifications in his Nobel Prize acceptance address in 1952: “We are dealing not merely with a new tool but with a new subject I have called simply nuclear magnetism. If you will think of the history of ordinary magnetism, the electronic kind, you will remember that it has been rich in difficult and provocative problems and full of surprises” [1]. Today applications of NMR span the range of science, from studying molecular structure through chemical shift analysis to probing the content of oil fields through porosity measurements.

NMR applications have also found their way into the field of biomedical technology, two of which will be the subject of this thesis. In the form of Magnetic Resonance Imaging (MRI) it has provided a non-invasive method for viewing biological structure and, to a degree, function. By using magnetic field gradients, atoms can be preferentially excited in a certain region of the body and frequency and phase information can be encoded. Fourier transforming these frequency- and phase-encoded signals yields a tomographic image of the target. The utility of MRI has increased tremendously in the last two decades, making it a routine imaging tool. Its various uses include diagnosis of pathologies, identification of tumors, monitoring blood flow, and studying brain function.

The atom of choice for physiological studies has typically been hydrogen because of its abundance in tissue in the form of water. The density of water vapor in the lung, however, is four orders of magnitude lower than that of water in tissue, reducing the signal to noise ratio (SNR) significantly [2]. Thus an unreasonable amount of time would be required to average the signal to obtain a satisfactory SNR. In addition, physiological motion artifacts (breathing, heart beats, etc.) and magnetic susceptibility variations near tissue increase the difficulty of employing these techniques.

The advent of so-called hyperpolarized noble gases shows great potential for lung imaging and characterization. Through the process of spin-exchange optical pumping, angular momentum from circularly polarized laser light is transferred via rubidium valence electrons to the nuclei of noble gases such as xenon (^{129}Xe) or helium (^3He). By preferentially populating one particular spin state of the noble gas nuclei, this technique can increase the net polarization of a sample of gas by a factor of 10^5 above thermal levels. This tremendous enhancement of bulk polarization can compensate for the relatively low density of the gas to yield highly enhanced SNR. Both gases are inert and therefore safe to inhale, making them suitable for *in vivo* lung studies, such as imaging of the human oral cavity [3] and lung [4].

Another application of NMR that has entered the biomedical realm relatively recently is the measurement of fluid diffusion. This technique is based on the ability to induce phase differences in a sample of atoms precessing in a constant magnetic field. By imposing field gradients, the spins can be dephased and rephased. If the nuclei do not move between the gradient pulses, the rephasing pulse refocuses all the spins (ignoring other relaxation effects), producing a detectable “echo” signal. If the sample can diffuse or flow, the spins are in a different spatial location during the rephasing pulse relative to their position during the dephasing pulse, causing attenuation of the spin echo due to incomplete refocusing. The degree of attenuation provides a measure of diffusivity. This free diffusion technique has been used to detect anisotropic diffusion in human white matter [5], as well as to detect post-stroke edemas much earlier than they are detectable by MRI [6].

If diffusion is limited by the presence of boundaries, however, diffusivity will change with time. For small diffusion times the molecules diffuse freely and the measured diffusivity is that of free diffusion. But as the time allowed for diffusion increases, the molecules will begin to feel the presence of the boundaries which will restrict their motion, decreasing the measured diffusivity. Knowledge of the diffusivity as a function of evolution time allowed for diffusion provides a measure of the surface area to volume ratio (S/V) of the porous medium, as well as its porosity. Thus if one were to use this technique on a sample of gas within the lungs, one could assess the

S/V ratio of the alveolar space, as well as the porosity of the lung parenchyma. These values would be helpful in diagnosing the severity of diseases such as emphysema, which is characterized by loss of alveolar surface [2]. This thesis describes the first attempt to measure time-dependent (restricted) diffusion from a gas in an animal.

This thesis begins with a discussion of the theory behind nuclear magnetic resonance and magnetic resonance imaging, spin-exchange optical pumping, and free and restricted diffusion. Following a description of the experimental methods, the results and a discussion of the implications and areas for future study are provided.

II THEORY

II.1 Nuclear Magnetic Resonance

Any nucleus with an odd number of nucleons will have a net magnetic dipole moment μ due to unmatched spins, given by [7]

$$\mu = g \left(\frac{\mu_N}{\hbar} \right) \mathbf{S} , \quad [1.1a]$$

$$\mu_N = \frac{e\hbar}{2M_p c} = 0.505 \times 10^{-23} \text{ erg / gauss} \quad [1.1b]$$

where \mathbf{S} is the spin angular momentum, M_p is the mass of a proton, and the Landé factor $g = 5.58$ for a lone proton, with different values for different nuclei. The quantity μ_N is called the nuclear magneton, and $\gamma = g\mu_N / \hbar$ is the gyromagnetic ratio, the ratio of magnetic moment to angular momentum. For our purpose we are interested in spin one-half particles, $s = \frac{1}{2}$, such that $m_s = +\frac{1}{2}, -\frac{1}{2}$.

When this magnetic dipole is placed in a uniform magnetic field $\mathbf{B} = B\hat{z}$, it will tend to precess about the field with a characteristic frequency. The torque felt by the magnetic moment $\mathbf{N} = \mu \times \mathbf{B}$ can also be written as $\mathbf{N} = d\mathbf{S}/dt$. Using [1.1a], we have $d\mu/dt = \mu \times \gamma\mathbf{B}$, the solution for which is the precession of μ about \mathbf{B} at the so-called Larmor frequency

$$\omega = \gamma B . \quad [1.2]$$

To follow a quantum mechanical approach, we first write the time-dependent Schrödinger equation for the state ξ :

$$i\hbar \frac{\partial}{\partial t} \xi = \hat{H} \xi , \quad [1.3a]$$

$$\hat{H} = -\hat{\mu} \cdot \mathbf{B} = -\mu_N \hat{\sigma} \cdot \mathbf{B} . \quad [1.3b]$$

The Hamiltonian is the energy of interaction between the magnetic moment and the stationary field. Here $\hat{\sigma}$ represents the Pauli spin matrices, but since $\mathbf{B} = B\hat{z}$, we have simply

$$\hat{H} = -\mu_N B \hat{\sigma}_z . \quad [1.4]$$

Using $\hat{\sigma}_z = \begin{pmatrix} 1 & 0 \\ 0 & -1 \end{pmatrix}$, and letting $\xi(t) = \begin{pmatrix} a(t) \\ b(t) \end{pmatrix}$, we have

$$\xi(t) = \begin{pmatrix} a \\ b \end{pmatrix} = \frac{1}{\sqrt{2}} \begin{pmatrix} e^{-i\omega t} \\ e^{+i\omega t} \end{pmatrix} \quad [1.5]$$

where ω is the Larmor frequency from above. The gyromagnetic constant γ is a function of the nucleus. Values of interest for us are those for ^1H and ^{129}Xe :

$$\gamma_{^1\text{H}} = 2.675 \times 10^4 \text{ rad / sec / gauss} = 42.58 \text{ MHz / T}$$

$$\gamma_{^{129}\text{Xe}} = 7.401 \times 10^3 \text{ rad / sec / gauss} = 11.78 \text{ MHz / T}$$

To find the eigenenergies of this system, we solve the time-independent Schrödinger equation

$$\hat{H}\xi = E\xi \quad [1.6]$$

using the same Hamiltonian from above. This gives the result

$$E = \pm \hbar\omega . \quad [1.7]$$

These two energies correspond to the magnetic moment lining up anti-parallel and parallel to the stationary field, respectively. When the moment is anti-parallel, $-\mu \cdot \mathbf{B}$ is a maximum, with energy $+\hbar\omega$, and when parallel $-\mu \cdot \mathbf{B}$ is a minimum, with energy $-\hbar\omega$. This splitting of energy due to the presence of \mathbf{B} is the nuclear Zeeman effect.

To simplify matters, we may consider a frame rotating at the Larmor frequency about the z - axis. This frame takes into account the precession of the atomic moment. If the lab frame is defined by the coordinate unit vectors $\hat{x}, \hat{y}, \hat{z}$, the rotating frame is defined by $\hat{x}', \hat{y}', \hat{z}$. While this moment is precessing in the uniform magnetic field, one can apply a transverse field perpendicular

to the plane defined by $\mu \equiv \mu \hat{y}'$ and \mathbf{B} ($\hat{y}'-\hat{z}$ plane) to change the angle θ between μ and the z – axis. But because μ is precessing about \mathbf{B} (or, equivalently, the z – axis) at the Larmor frequency, this transverse field \mathbf{B}_\perp will be perfectly resonant if it oscillates at the Larmor frequency. Thus it is of the form

$$\mathbf{B}_\perp = B_\perp \cos(\omega t) \hat{x} \quad [1.8]$$

or simply $B_\perp \hat{x}'$. Since this field is perpendicular to both μ and \mathbf{B} , it can be thought of as exerting a torque $\mathbf{N} = \mu \times \mathbf{B}_\perp$ in the μ - \mathbf{B} ($\hat{y}'-\hat{z}$) plane.

In the rotating frame, the transverse field, also known as the RF field, is constant. If the RF field is pulsed for time t_p , we know that

$$\theta = \gamma B_\perp t_p . \quad [1.9]$$

Once the RF pulse ends, the bulk polarization (the sum of all the moments) will undergo two distinct processes. In one, the component of polarization along the z – axis returns to its original value following an exponential time course (for more a more detailed discussion, see Abragam [8]). The time constant for this event is called T_1 , the longitudinal or spin-lattice relaxation time.

In addition to this effect, atomic interactions and variations in the magnetic field at each spin can cause different spins to precess slightly faster or slower than ω . This frequency spreading leads to the development of phase differences between individual moments, causing them to fan out in the transverse plane. This dephasing process reduces the net transverse polarization, for any particular spin has a chance of being effectively canceled by another 180° apart. The time constant for this process is called T_2 , the transverse or spin-spin relaxation time. This relaxation mechanism is diagrammed schematically in Figure II.1.

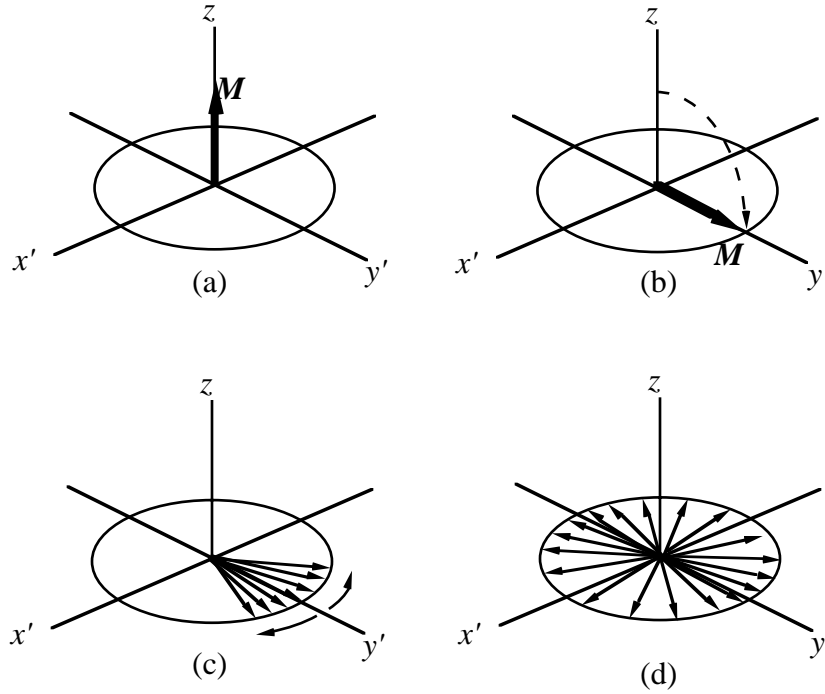


Figure II.1. T_2 relaxation mechanism. (a) Magnetization lies along the z - axis. (b) Magnetization is tipped into x' - y' plane. (c) Individual spins begin to dephase due to atomic interactions, etc. (d) Spins are completely dephased.

There is also a third parameter called T_2^* that takes into account fixed inhomogeneities in the magnetic field due to magnetic susceptibility variations, for example, as well as other T_2 effects [9]. Due to the nature of these relaxation processes, the following is always true:

$$T_2^* \leq T_2 \leq T_1 \quad [1.10]$$

If a coil of wire is placed around the target, the alternating magnetic flux through the coil from the spinning moments gives rise to a detectable NMR signal at the Larmor frequency. The signal detected due to precession in the transverse plane is called the free induction decay (FID). Its strength immediately following the RF pulse is proportional to the density of spins, the transverse component of the magnetic moments, the *quality factor* (Q) of the pick-up coils, etc. The duration of the FID is governed solely by T_2 , since T_1 does not affect transverse magnetization. Thus the signal will decay within an exponential envelope. If the pulse occurs at $t = 0$, the signal $S(t)$ at $t = 0^+$ is

$$S(t) = S_0 \sin(\theta) \cos(\omega t) e^{-\frac{t}{T_2^*}} \quad [1.11]$$

where T_2^* more generally takes into account dephasing due to atomic interactions and field inhomogeneities. Thus the largest signal is produced with a 90° flip angle.

If the RF is pulsed multiple times, the signal could be attenuated due to saturation of longitudinal polarization. If the repetition time $T_r < T_1$, then the polarization will not fully build up before it is tipped again. In the limit $T_r \rightarrow 0$, the signal will disappear because polarization will never rebuild. Thus for multiple pulses we have

$$S(t) = S_0 \sin(\theta) \cos(\omega t) e^{-\frac{t}{T_2^*}} \left(1 - e^{-\frac{T_r}{T_1}} \right) \quad [1.12]$$

Because we will later be interested in measuring these relaxation rates, it is worthwhile to discuss how they are measured. One way T_1 is measured is by the inversion-recovery method [10]. In this process, the magnetization is first inverted with a 180° pulse. If its original value was $M\hat{z}$, its value immediately after the π pulse is $-M\hat{z}$. Through spin-lattice relaxation, the magnetization recovers to its original value by relaxing back along the z – axis. If a 90° pulse is applied before the magnetization fully recovers, it can be put into the transverse plane along the \hat{y}' – axis and measured. The magnetization is then allowed to recover by waiting a sufficient amount of time ($\sim 5 T_1$ periods), and the process is repeated. In this way the degree of polarization is interrogated at varying times during the decay. The polarization should start at $-M\hat{z}$ and rise along an exponential time course through zero to $M\hat{z}$. Fitting a curve to this data and extracting the rate constant gives T_1 . This method is illustrated in Figure II.2.

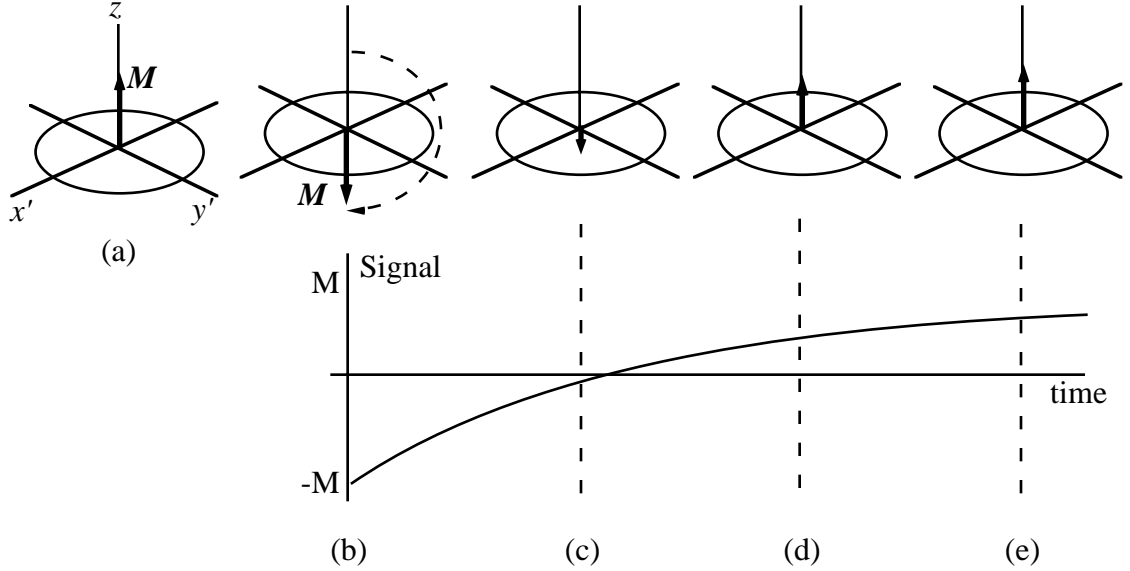


Figure II.2. Inversion-recovery method for measuring T_1 . (a) Magnetization lies along the z – axis. (b) 180° RF pulse tips M to $-M\hat{z}$. (c) - (d) Magnetization is relaxing back. Interrogation with a 90° pulse at any time would give signal as shown. (e) M has recovered to $M\hat{z}$.

Another common way to measure T_1 is called the saturation-recovery method [11]. This method is based on the fact that the polarization measured between successive pulses separated by a short time delay will saturate, as discussed above. For short delays, the measured signal will be small, but at delay times much greater than T_1 the signal strength will level off to that of a single pulse. The exponential asymptotic behavior in between these two extrema gives a measure of T_1 . This method is preferable when T_1 is long, because with inversion-recovery one has to wait $\sim 5 T_1$ periods to allow the polarization to fully recover between measurements. The saturation-recovery method does not require this long delay.

Measuring T_2 is more difficult because of the presence of local field inhomogeneities. One method involves using the Carr-Purcell-Meiboom-Gill (CPMG) spin echo technique, named after its developers [12]. In this process, the magnetization is first tipped to the \hat{y}' – axis with a 90° pulse along \hat{x}' (denoted as 90_x°). Through T_2^* relaxation, phases will start to decohere, resulting in a fanning out of magnetic moments in the \hat{x}' – \hat{y}' plane. This decoherence is caused by both homogenous spreading due to energy interchanging reactions between neighboring spins (T_2), as well as inhomogenous spreading due to local field inhomogeneities (T_2^*). If a π pulse is

then applied in the \hat{y}' direction (180_y°), the moments will be rotated around the \hat{y}' -axis such that T_2^* spreading is reversed and spins tend to move towards realignment. Spreading due to T_2 , however, will continue to occur; thus this process isolates T_2 relaxation. The component of transverse polarization spreading due to T_2^* will be re-focused along the \hat{y}' -axis, for it will cohere at the same rate that it decohered. These moments will re-align simultaneously, producing a measurable signal. This “echoed” signal is called a *spin echo*.

After the first echo the spins are flipped in the opposite direction (180_{-y}°) and emit another echo. But this echo will be attenuated compared to the preceding one because of T_2 loss. A measurement of the logarithm of echo strength versus time gives a straight line, the slope of which is T_2 . In actual practice, only every other echo is used in the calculation of T_2 , starting with the second. If the RF is not exactly 180° , the spins will not lie completely in the \hat{x}' - \hat{y}' plane. A second pulse, equal and opposite to the first, will put the spreading moments exactly back in the \hat{x}' - \hat{y}' plane and give rise to a true echo. Figure II.3 illustrates this method.

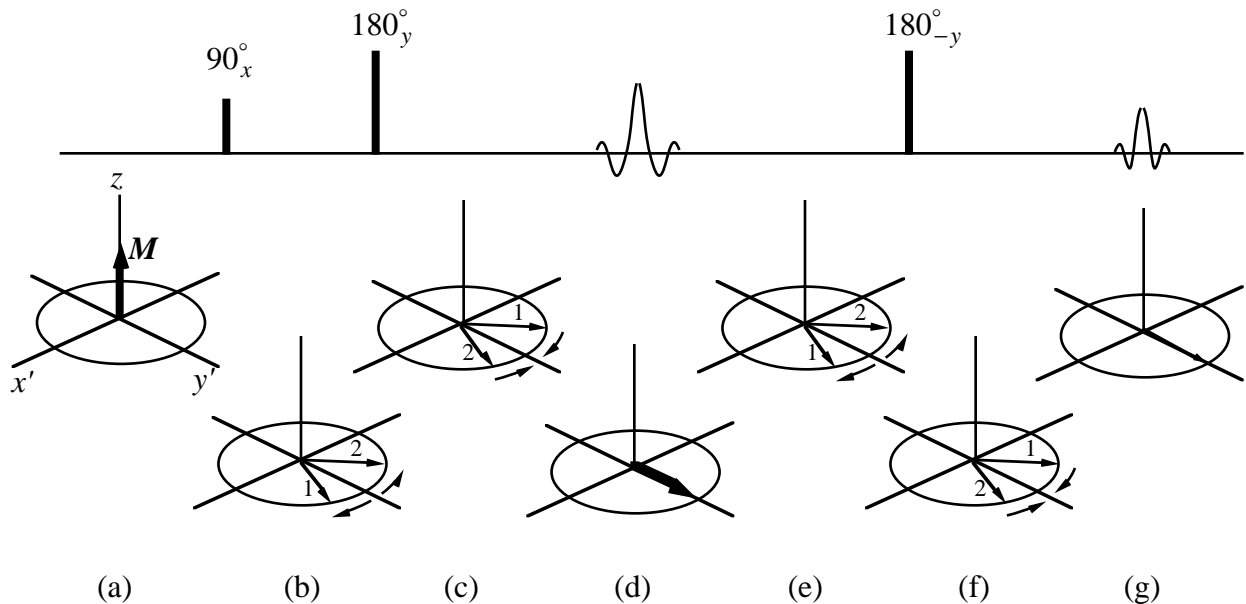


Figure II.3. CPMG method for measuring T_2 . (a) Magnetization lies along the z -axis. (b) A 90_x° pulse puts the magnetization in the transverse plane, where it starts to dephase. (c) A 180_y° pulse flips the spins so that they start to re-cohere. (d) The spins refocus and produce a spin echo. (e) Spins keep dephasing. (f) After an opposite 180_{-y}° pulse spins start to re-cohere again. (g) Another spin echo is created, attenuated relative to the first, due to homogeneous (T_2) spreading.

Although an individual magnetic moment may prefer to be in the lower energy state in a constant magnetic field ($-\hbar\omega$), a bulk ensemble of magnetic moments will have a fractional occupation of both states. This distribution is the result of thermal agitations. If the thermal energy of the sample is large compared to the difference in energies between the spin states, as usually is the case, both states will be nearly equally occupied. There will only be a small excess of uncanceled spins pointing along \mathbf{B} , giving the sample a small bulk polarization.

We can calculate this polarization explicitly. The Boltzmann factor is

$$e^{-\frac{E}{k_B T}} = e^{\frac{\mu \cdot \mathbf{B}}{k_B T}} \quad [1.13]$$

where $k_B = 1.380 \times 10^{-23}$ J / K. Denote the number of atoms with moments pointing in one direction (up) as N_\uparrow and the number pointing in the other direction (down) as N_\downarrow . The ratio of their probability of occupancy is the ratio of their Boltzmann factors:

$$\eta \equiv \frac{p(N_\uparrow)}{p(N_\downarrow)} = e^{-\frac{\Delta E}{k_B T}}. \quad [1.14]$$

The bulk polarization is given by

$$P = \frac{N_\uparrow - N_\downarrow}{N_\uparrow + N_\downarrow} = \frac{\eta - 1}{\eta + 1} \quad [1.15]$$

Since $\Delta E \ll k_B T$, we can expand the exponential in a Taylor series:

$$P \approx \frac{\left(1 - \frac{\Delta E}{k_B T}\right) - 1}{\left(1 - \frac{\Delta E}{k_B T}\right) + 1} = \frac{-\frac{\Delta E}{k_B T}}{2 - \frac{\Delta E}{k_B T}} \quad [1.16]$$

The $\frac{\Delta E}{k_B T}$ in the denominator is small, so using $E = -\mu \cdot \mathbf{B}$ we have the useful relation

$$P \propto \frac{B}{T} \quad [1.17]$$

Thus the polarization of a thermal sample is proportional to the applied magnetic field. In a clinical MRI apparatus, fields on the order of a few tesla are used to create a detectable polarization ($\sim 10^{-5}$) between the states of ^1H in $^1\text{H}_2\text{O}$.

We will later be interested in the polarization of xenon gas, so it is worthwhile to calculate the polarization of thermal Xe, compared to $^1\text{H}_2\text{O}$, as an example. It should be noted that of the noble gas nuclei, only ^{129}Xe and ^3He are spin one-half. Of natural abundance xenon, 26% is ^{129}Xe . Our experiments were often carried out with ^{129}Xe , so we will restrict ourselves to its consideration. As given above, $E/B = 11.78 \text{ MHz / T}$ in frequency terms for ^{129}Xe . At an operating field of 1.5T, we have $P = 1.44 \times 10^{-6}$, a spin excess of about one in a million, or 0.0001%. A similar calculation for H_2O ($E/B = 42.58 \text{ MHz / T}$) gives a polarization of $P = 5.11 \times 10^{-6}$. Although this value is not much greater than that of Xe, the actual bulk magnetization, which takes into account spin density ρ , magnetic moment μ , and spin abundance as well,

$$M = P\mu\rho \quad [1.18]$$

is much larger. The magnetic moment of H_2O is 3.6 times greater than that of Xe, the spin density of liquid H_2O is four orders of magnitude larger than Xe gas, and the abundance of ^1H in $^1\text{H}_2\text{O}$ is 200%, compared to the 26% natural abundance of ^{129}Xe , giving a water magnetization $\sim 10^5$ times greater than that of Xe. Hence the greater difficulty of doing gaseous Xe NMR.

II.2 Magnetic Resonance Imaging

One useful NMR technique is the ability to localize the signal such that a specific region of the sample can be studied. Suppose we impose a magnetic field with a constant gradient of the form

$$\mathbf{B}_1 = \frac{\partial B}{\partial z} \mathbf{z} \quad [2.1]$$

on top of the constant \mathbf{B} field. At $z > 0$, the field is greater than that in the $z = 0$ plane, and because field strength and frequency are proportional (as in [1.2]), atoms will precess faster. At $z < 0$, the field is less than that in the $z = 0$ plane, so the atoms will precess slower. If an RF pulse is now applied, the region of study is localized to those spins precessing at frequencies near that of the RF pulse. Thus this slice select field serves to limit excitation to a specified plane of constant z . The thickness of this plane depends on the shape and duration of the excitation pulse. A square (hard) pulse in the time domain will produce a sinc-shaped pulse in the frequency domain, whereas a sinc (soft) pulse in the time domain will produce a square shaped pulse in the frequency domain, since the square and sinc functions are related through a Fourier transform. Thus in order to excite a narrow distribution of frequencies, a sinc-shaped RF pulse is used. The narrower the desired frequency band, the longer the RF pulse must be.

This slice selection in combination with two-dimensional encoding fields can be used to create MR images. The imposition of \mathbf{B}_1 during the RF pulse localizes excitation to a plane in z . Since the RF pulse must have a finite duration, there will be some spread in excited frequencies. Thus the slice-select gradient is often reversed after the RF pulse in order to cancel this frequency-spreading effect. Now suppose a gradient field of the form

$$\mathbf{B}_2 = \frac{\partial B}{\partial y} \mathbf{z} \quad [2.2]$$

is pulsed. This field will phase encode the spins such that all the spins in a column of constant y will have the same phase, but neighboring columns will be phase-shifted relative to one another because of the positionally variant strength of the pulse. After this phase encoding gradient field, a third gradient field is applied during the acquisition, called the read gradient. In this case the field would be

$$\mathbf{B}_3 = \frac{\partial B}{\partial x} \mathbf{x} . \quad [2.3]$$

This frequency encoding gradient field creates a shift in frequency in the x direction during the readout. This sequence is repeated several times, each with a different value of \mathbf{B}_2 , corresponding to a different value of encoded phase. This basic imaging sequence is shown schematically in Figure II.4:

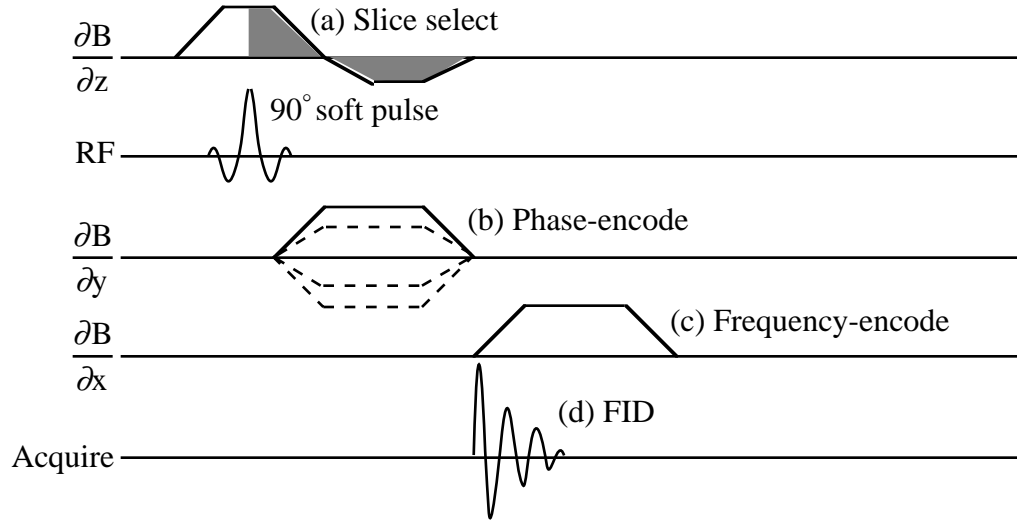


Figure II.4. Basic MR imaging sequence. (a) The slice select gradient $\partial B/\partial z$ allows the RF pulse to selectively excite spins within a chosen z plane. After the RF pulse it is reversed to cancel frequency spreading effects. (b) The phase-encode gradient $\partial B/\partial y$ encodes phase into the spins along columns of constant y . Changing the magnitude of $\partial B/\partial y$ changes the amount of phase encoding. (c) The read gradient $\partial B/\partial x$ encodes a spatially-dependent frequency into the spins. (d) The FID is acquired.

This process creates a two-dimensional encoding of the acquired signal in the selected z plane in frequency-space (k -space). Fourier transforming this signal will yield a two-dimensional density map of the desired slice. Increasing the number of sequence repetitions increases the resolution of the image. *In vivo* MR images are weighted by local variations in T_1 and T_2 . These variations can be utilized to create greater contrast between different types of tissue.

II.3 Spin-exchange Optical Pumping

In spin-exchange optical pumping, a glass cell is prepared free from paramagnetic impurities in its walls. It is filled with a mixture of the noble gases helium or xenon (in our case, ^{129}Xe), as well as nitrogen and the alkali-metal rubidium (Rb). Rb is a favorite in this process

because it has a high vapor pressure, allowing operation at reasonable temperatures. In addition, it has a resonance line at 794.7 nm, conveniently obtained by many tunable light sources, including diode and titanium-sapphire lasers. The cell is kept at a constant temperature by an oven to create Rb vapor pressure from a few drops of metallic Rb chased into the cell. The presence of pure Rb necessitates a carefully-maintained oxygen-free environment to prevent oxidation.

Several watts of left-circularly polarized light at 794.7 nm excites Rb electrons from the spin down sublevel of the $^2S_{1/2}$ state to the spin up sublevel of the $^2P_{1/2}$ state. The optical pumping rate γ_{opt} is linearly dependent on laser power [13]. Starting with unpolarized Rb vapor, we have

$$P_{\text{Rb}} = \frac{\gamma_{opt}}{\gamma_{opt} + \Gamma_{SD}} \left[1 - e^{-(\gamma_{opt} + \Gamma_{SD})t} \right] \quad [3.1]$$

where Γ_{SD} is the bulk spin destruction rate, which depends on relaxation due to collisions with wall impurities, etc. The steady-state polarization reflects an equilibrium between photon absorption and spin destruction.

Collisions with noble gas atoms rapidly mix the sublevel populations between the two excited states (up and down). Quenching collisions with nitrogen atoms de-excite the Rb electrons to both sublevels of the $^2S_{1/2}$ state with nearly equal probability. This mechanism also prevents photons from being reemitted, for their polarization after a few scatterings would be randomized. This radiation trapping of unpolarized photons could effectively *depump* the Rb atoms, drastically reducing the buildup of polarization. Before absorbing the photon the electron spin angular momentum of an Rb atom with an electron in the spin down ground state is $-\hbar / 2$. After excitation and quenching, the average angular momentum is 0, since both ground states are equally populated. Thus each photon deposits on average $\hbar / 2$ of angular momentum to the Rb atoms.

The final process is the transfer of polarization from Rb to ^{129}Xe . At typical pressures (a few atm Xe), binary collisions between Rb and ^{129}Xe atoms are the dominant form of polarization exchange [14]. Spin-dependent collisions, described by a Rb- ^{129}Xe interatomic potential $V_1(\mathbf{R})$, constitute the means of spin transfer and relaxation:

$$V_1(\mathbf{R}) = \gamma(R)\mathbf{N} \cdot \mathbf{S} + A(R)\mathbf{I} \cdot \mathbf{S} \quad [3.2]$$

where \mathbf{R} is the interatomic separation, \mathbf{S} is the Rb electron spin, \mathbf{I} is the ^{129}Xe nuclear spin, γ and A are variable coefficients, and \mathbf{N} is the rotational angular momentum of the Rb- ^{129}Xe atomic pair. This potential is in addition to spin-independent interactions, $V_0(\mathbf{R})$, which under standard conditions determine classical collision trajectories. The first term of $V_1(\mathbf{R})$ is the spin-rotation interaction, arising from magnetic fields caused by the motion of charges during the collision. This effect is a relaxation mechanism for the Rb electron spin. The second term, the isotropic hyperfine interaction, denotes the transfer of polarization between the Rb electrons and the ^{129}Xe nuclei. The rate equations describing the evolution of the Rb electron and ^{129}Xe nuclear spin polarizations are:

$$\begin{aligned} \frac{d\langle S_z \rangle}{dt} &= -\Gamma_a(\gamma)\langle S_z \rangle - \Gamma_a(A)[\langle S_z \rangle - \langle I_z \rangle] \\ \frac{d\langle I_z \rangle}{dt} &= \Gamma_b(A)[\langle S_z \rangle - \langle I_z \rangle] \end{aligned} \quad [3.3]$$

where the Γ s are characteristic rates. The first term of $d\langle S_z \rangle/dt$, dependent on γ , is due to the spin-rotation interaction; its negative sign refers to its nature as a relaxation mechanism. The second term, dependent on A , is due to the isotropic hyperfine interaction; it represents a transfer of polarization from Rb to ^{129}Xe nuclei. Since $\Gamma_b = k_{SE}[\text{Rb}]$ and k_{SE} for Rb- ^{129}Xe spin exchange is $3.6 \times 10^{-16} \text{ cm}^3 \text{ sec}^{-1}$ [15], a Rb density of greater than 10^{11} cm^{-3} is required to achieve reasonable pump-up times (on the order of one hour). In the steady-state, with $d\langle I_z \rangle/dt = 0$, we can see that the Xe atomic polarization will equal that of the Rb electrons, assuming the absence of any relaxation mechanism other than the one already mentioned.

Other sources of Xe spin relaxation include local field inhomogeneities. These can be caused by paramagnetic impurities in the cell wall or the presence of oxygen, a paramagnetic molecule. Although O_2 has 16 electrons, their most preferable state is not one of mutual spin cancellation; hence the paramagnetism. In the neighborhood of a paramagnetic particle, the local

field is highly inhomogeneous. Xe atoms passing by will be disturbed by the differences in magnetic field, scrambling net polarization. Xe collisions with the cell walls are another source of polarization loss, although they can be minimized by careful preparation and cell coating. We coat the cells with a solution of octadecyltrichlorosilane (OTS, Figure II.5). The silane group ($-SiCl_3$) binds to the glass wall, allowing a long hydrocarbon tail to extend outward, providing a cushion of sorts to prevent the atoms from colliding with the cell surface. For a discussion of cell preparation techniques, see Chupp [16].

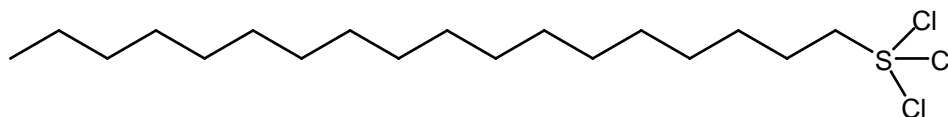


Figure II.5. Octadecyltrichlorosilane (OTS). Used to coat glass cells to increase T_1 .

The spin-exchange optical pumping technique can yield an increase in bulk Xe polarization of five orders of magnitude, such that the degree of bulk magnetization is comparable to that of water. An important difference between hyperpolarized gas and thermal gas is that the polarization of hyperpolarized gas is not easily renewable in a sample. Once spins are tipped with an RF pulse, they will return to their equilibrium *thermal* polarization. Thus NMR pulse sequences have to be designed differently for hyperpolarized samples. To determine the degree of hyperpolarization, we use the fact that the signal from the pick-up coils is proportional to the polarization. Knowing the thermal polarization (as calculated before), we can tip the hyperpolarized sample with a small known tip angle and measure its signal. Comparing that signal to the thermal signal gives the degree of polarization, which can reach several percent. This large enhancement of polarization compensates for the low density of the gas, providing more than adequate SNR.

II.4 Free Diffusion

NMR techniques can also be used to study the diffusion of a fluid. This technique is based on the ability to spatially encode the spins such that atoms may be labeled and tracked without

perturbing their motions. Such spatial encoding may be accomplished by means of a gradient spin echo, originally developed by Carr and Purcell [12]. This sequence begins with a 90° pulse, putting all spins in the transverse plane. A magnetic field gradient is then applied to encode phase in the spins in a spatially dependent way. In the middle of the gradient, the spins are flipped 180° , such that the gradient now causes spins to cohere, rather than decohere. Assuming a non-diffusive sample, no field inhomogeneities, and a T_1 and T_2 much longer than the time scale of the experiment, all the spins will refocus and produce a spin echo. This idea is similar to that used by the CPMG technique to measure T_2 (Figure II.3), except that in this case the dephasing is manually controlled.

If the sample is diffusive, however, the spins will diffuse while the gradient is on, such that at the end of the gradient they will be positionally mixed. Because the spins are now distributed slightly randomly, they will not refocus exactly, producing an attenuated spin echo. The stronger the gradient, the more phase-shifted the spins will be, and the less they will cohere after diffusion. The degree of attenuation depends on the diffusivity of the fluid and strength of the gradient. Thus varying the gradient strength and measuring the subsequent attenuation provides a measure of the diffusivity, D , of the sample.

The disadvantage of this method, however, is that one cannot measure diffusion in a *time-dependent* manner. The constant gradient technique is only useful for measuring the diffusion for one particular allowed diffusion time. To allow for time-dependent study, the single gradient must be divided into two gradients – one to encode positional information and the other to decode – with the same 180° pulse in between. They can then be separated by a variable delay time such that the diffusion time may be controlled. Such pulse sequences, including the pulsed gradient spin echo (PGSE) and its variants, were first developed by Stejskal and Tanner [17]. In PGSE, the 90° pulse that puts the polarization into the transverse plane is immediately followed by a short gradient pulse (of magnitude g and duration δ), marking spins' position within the sample. After a variable delay Δ , during which a 180° pulse is given, an identical gradient is pulsed. The diffusive attenuation now depends on the strength of the gradient pulses and diffusion time, which

are controlled, and the rate of diffusion, which can thus be measured. This sequence is shown schematically in Figure II.6.

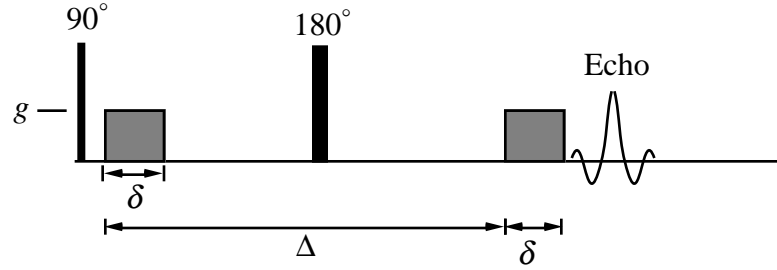


Figure II.6. Pulsed gradient spin echo (PGSE) sequence. Spins are tipped into the transverse plane with a 90° pulse. A diffusion encoding gradient (shown in gray) with magnitude g and duration δ gives spins a spatially-dependent phase. Diffusing spins are allowed to evolve for a period D during which a 180° pulse is applied to flip the spins. An identical gradient is then applied, refocusing the spins and giving rise to a gradient echo.

Any PGSE experiment can be divided into three parts: preparation, evolution, and observation [18]. During the preparation period, the spins are given a spatially-dependent phase encoding $\phi(\mathbf{r}) = \mathbf{k} \cdot \mathbf{r}$ where \mathbf{k} is the wavevector, defined by the applied field gradient

$$\mathbf{k} = \gamma \int_T \mathbf{g}(t) dt \quad [4.1]$$

For a square or half-sine shaped gradient, this becomes $\mathbf{k} = \gamma \mathbf{g} \delta$ or $\mathbf{k} = \gamma \mathbf{g} \delta (2/\pi)$, respectively, where δ is the duration of the applied gradient and γ is the gyromagnetic ratio. The spins are then allowed to diffuse for a time period Δ . Following this evolution period, the spin echo is formed, the spins are observed, and their NMR signal M is measured. In an infinite homogeneous isotropic medium with diffusion coefficient D , the relation between M , Δ , and \mathbf{k} is

$$-\ln \left[\frac{M(\mathbf{k}, \Delta)}{M(0, \Delta)} \right] = \mathbf{k}^2 D \Delta . \quad [4.2]$$

Effects of T_1 and T_2 relaxation are accounted for in the normalization of $M(0, \Delta)$. The slope of a plot of $\ln[M]$ vs. $\mathbf{k}^2 \Delta$ yields the diffusion constant D . When measuring D at constant Δ , variance of \mathbf{k} should take the form of varying the gradient strength g rather than its duration δ .

The shorter the pulse, the less error will be introduced due to diffusion during the encoding or decoding. In freely diffusive experiments, the value of D calculated should be independent of Δ .

The systems of interest in our case are heterogeneous – the gas must diffuse in porous media (*e.g.*, randomly packed glass beads) or lung alveoli. In this case, diffusion will be time-dependent, since contact with boundaries will reduce the rate of diffusion. Hence the motivation for pulsed gradients. In addition, field inhomogeneities at the gas-bead or gas-tissue interface can be quite large. These so-called background gradients, \mathbf{g}_0 , further dephase the transverse polarization, deleteriously affecting the SNR of the diffusion measurement. Heterogeneous systems are also characterized by a very short T_2 . Thus even for short diffusion times, T_2 relaxation will destroy polarization too quickly for a diffusion measurement. To counteract this phenomenon, a variation to the PGSE called pulsed gradient stimulated echo (PGSTE) was developed [19] (Figure II.7). The 180° pulse from the PGSE is replaced by two 90° pulses. The effect of the 90° pulse is to lift the polarization out of the transverse plane, where it can be rapidly destroyed by T_2 , back onto the longitudinal axis, where its relaxation is governed by the longer T_1 . Thus the spins will not be affected by background gradients after the 90° pulse. The final 90° pulse puts magnetization back into the transverse plane, where it is refocused with the second gradient.

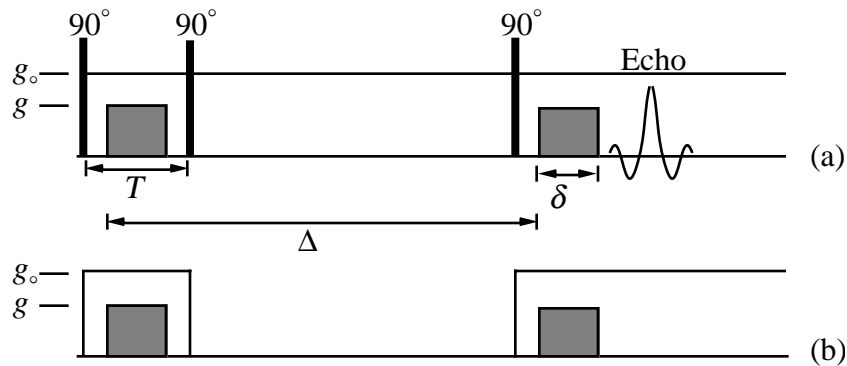


Figure II.7. Pulsed gradient stimulated echo (PGSTE) sequence. (a) The true field representation. (b) The effective field representation. The second 90° pulse puts magnetization back along the z – axis, protecting it from T_2 dephasing.

The “true” representation of the pulse (II.7a) illustrates the actual fields that are present and the gradient signals sent. The “effective” representation (II.7b) is the gradient or field that an atom would experience. For example, a positive gradient following a π pulse is effectively the same as a negative gradient. The spins only feel the effect of background gradients for the duration T , rather than during the whole experiment. Thus \mathbf{g}_0 disappears from the effective field representation after the second 90° pulse. For this pulse sequence, the measured attenuation becomes [20]

$$-\ln\left[\frac{M(\mathbf{k}, \Delta)}{M(0, \Delta)}\right] = D\left\{\left(\Delta - \frac{\delta}{3}\right)\mathbf{k}^2 + \frac{1}{T}[2T\Delta - \vartheta(\delta)]\mathbf{k}\mathbf{k}_0 + \left(\Delta - \frac{T}{3}\right)\mathbf{k}_0^2\right\} \quad [4.3]$$

where $\vartheta(\delta)$ denotes a function of the time interval δ and other variable delay times (not shown). In addition, $\mathbf{k}_0 = \gamma\mathbf{g}_0T$. The terms depending on the background gradient \mathbf{k}_0 and the cross term between the background gradient and the applied gradient $\mathbf{k}\mathbf{k}_0$ can complicate analysis of the data. The existence of the \mathbf{k}_0^2 term produces a falsely higher attenuation measurement. The existence of the cross term and its dependence on Δ makes the $\ln[M]$ vs. $\mathbf{k}^2\Delta$ curve appear curved. This problem could be accounted for if the background gradient \mathbf{k}_0 were known; unfortunately their spatial variance is wide in heterogeneous media.

To try to alleviate these problems, a refinement to this sequence was made by Cotts *et al.* [21] and Karlicek and Lowe [22]. They employed a series of π pulses with intervening gradients of alternating sign instead of the single gradient pulse. The advantage to this method is that the spins keep getting flipped so that any decoherence due to background gradients will be refocused more often. It also reduces the amount of time the spins stay in any particular background gradient. A further benefit is the ability to build large gradients without long gradient pulses. The shift in wavenumber \mathbf{k} depends on the strength g and duration δ of the pulse. Since the strength of the pulse is limited by the instrument’s gradient coils, the time interval should be minimized for the same reasons as stated above. In practice, there is a limit to the shortness of δ as well, determined by instrumentation and gradient coil design.

The sequence we use was developed by Latour *et al.* [18] and employs this method for reducing the effect of background gradients (Figure II.8).

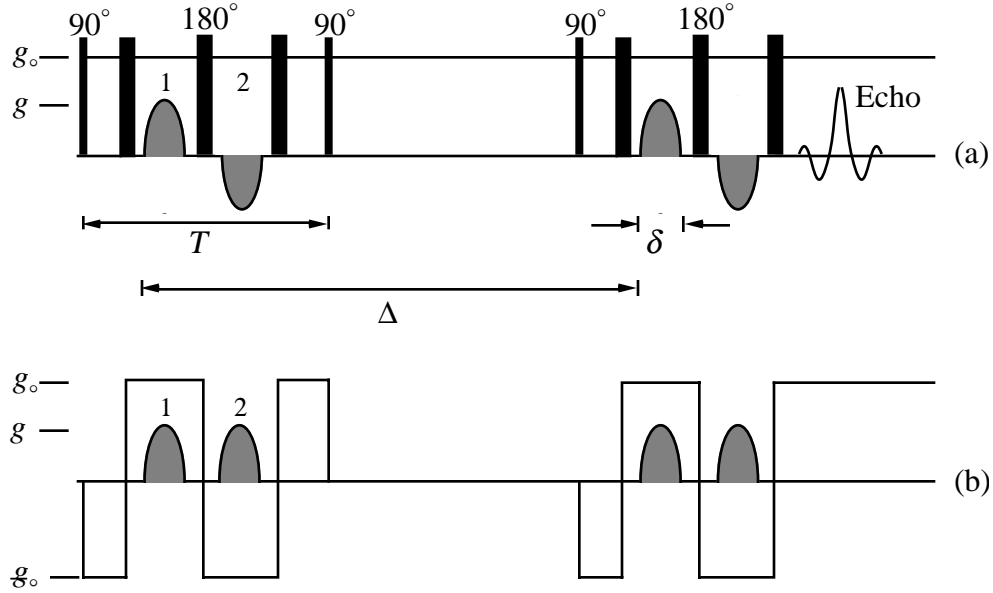


Figure II.8. Bipolar PGSTE with $n = 2$. (a) The true field representation. (b) The effective field representation. Dividing a single phase-encoding gradient into a pair of gradients of opposite sign separated by a 180° pulse reduces the effect of background gradients.

The attenuation from this sequence is

$$-\ln \left[\frac{M(\mathbf{k}, \Delta)}{M(0, \Delta)} \right] = D \left\{ \left[\Delta - \frac{\delta}{4n} - \frac{T}{3n}(n-1) \right] \mathbf{k}^2 + \left[\frac{T}{6(n+1)^2} \right] \mathbf{k}_0^2 \right\} \quad [4.4]$$

which is corrected for half-sine shaped gradients, rather than the more difficult-to-produce square pulses. In this case, $\mathbf{k} = n\gamma\mathbf{g}\delta(2/\pi)$ for n even. The advantage of this sequence over II.7 is apparent: the cross term disappears and the \mathbf{k}_0^2 term is reduced and no longer depends on Δ . In general, the background gradients will not be uniform, as we have assumed in the above derivation. But if the distance an individual spin travels before it is refocused is kept small, it will experience a uniform local field. Controlling n allows us to control its diffusion time through the non-uniform field.

A disadvantage to the PGSTE sequence is the large number of spin echoes generated by the alternating gradients. These spin echoes overlap with the stimulated echo and can deleteriously affect measurement of D . This effect increases with increasing n . Barker and Mareci [23] discuss the reduction of these effects through the techniques of phase cycling and the use of crusher gradients. The chosen value of n reflects a balance between these opposing considerations.

II.5 Restricted Diffusion

Fitting a line to a $\ln[M]$ vs. $\mathbf{k}^2\Delta$ plot gives the diffusion constant D . This process can be repeated several times with varying Δ to obtain a plot of D vs. allowed diffusion time. For a sample subject to free diffusion, D should not vary with time, but the situation changes in heterogeneous media. When diffusion is restricted, D will change with time because the fluid will feel the presence of the boundaries. To understand this effect, we may start with the Einstein relation for diffusion in three dimensions:

$$D(t) = \frac{\langle r^2(t) \rangle}{6t} \quad [5.1]$$

where $\langle r^2(t) \rangle$ is the mean square displacement of fluid molecules. In a freely diffusive sample, $D(t) = D_0$, the diffusion constant of the bulk fluid. In the presence of boundaries, however, $D(t)$ decreases with time from its initial value D_0 .

We define the diffusion length to be

$$l_D \equiv \sqrt{D_0 t} \quad [5.2]$$

and note that at early times, only fluid atoms within l_D from the walls will notice their presence. The fraction of atoms in this region is $l_D S/V$, where S and V are the surface area and volume of the porous space, respectively. It can be shown that at early times $D(t)$ deviates from D_0 according to [24]

$$\frac{D(t)}{D_0} = 1 - \frac{4}{9\sqrt{\pi}} \frac{S}{V} \sqrt{D_0 t} + \vartheta(D_0 t) . \quad (t \text{ small}) \quad [5.3]$$

We immediately see that at $t = 0$ the restricted diffusion rate matches that of free diffusion, as expected. For short times, the restricted diffusion rate depends solely on the S/V ratio of the pores, a very useful result.

The diffusion length also determines the minimum pore size that can be studied. If l_D is larger than the pore size (for the smallest observable diffusion time), then the microstructure will not be able to be resolved. This limitation is known as a breakdown of the “narrow pulse approximation”, the assumption that the encoding gradients are applied for a time period much less than characteristic diffusion times. This approximation is necessary for the simplifications underlying PGSE techniques and their variants. It can be shown [25] that the approximation breaks down if the diffusion during the gradient pulse $\sqrt{D_0 \delta} \geq 0.14 a$, where a is the average diameter of the pores. To circumvent this problem, either the diffusion rate must be lowered or better coils and instrumentation must be developed to decrease δ .

As time grows large, the fluid atoms can sample the connectivity of the pore space (*i.e.*, diffuse between pores). The diffusion constant approaches an asymptotic value dependent on this connectivity [26]:

$$\frac{D(t)}{D_0} = \frac{1}{\alpha} + \vartheta(t^{-1}) \quad (t \text{ large}) \quad [5.4]$$

where α is the tortuosity of the pore space. Tortuosity is a measure of the constrictions and directional changes in the connective passages [27]. This measure is valuable in calculating properties of porous media such as conductivity and permeability. For example, porosity ϕ (fractional volume associated with pore space) is directly proportional to tortuosity [28]. Thus a measurement of time-dependent restricted diffusion gives us information about the microgeometry of a porous medium, including the S/V ratio of its pores and its overall tortuosity and porosity.

To calculate the diffusion coefficient for an atom diffusing through a mix of gases, one must first know the diffusion coefficient for the atom diffusing through each of the gases individually. For atom A diffusing through gas B , the diffusion coefficient for A is

$$D_{A-B} = \frac{1}{3} \lambda_A \bar{v}_A, \quad [5.5a]$$

$$\lambda_A = \frac{1}{n_B \sigma_A} \quad [5.5b]$$

where λ_A is the mean free path of atom A , \bar{v}_A is its average velocity, n_B is number density of gas B , and σ_A is the cross section of A scattering from B . The scattering cross section is given by πd^2 where d is the diameter of the atom or molecule [29]. By the ideal gas law

$$p = nk_B T \quad [5.6]$$

where p is pressure and T is temperature. Thus at a constant temperature, the diffusion coefficient scales inversely with pressure.

If there are p_A atmospheres of gas A and p_B atmospheres of gas B , and if D_{A-A} represents the diffusion coefficient of A diffusing through A (at 1 atm) and D_{A-B} represents the diffusion coefficient of A diffusing through B (at 1 atm), then

$$\frac{1}{D_A} = \frac{p_A}{D_{A-A}} + \frac{p_B}{D_{A-B}} \quad [5.7]$$

so diffusion coefficients add in reciprocal [30].

III METHODS

III.1 Human Inhalation Cart

The availability of hyperpolarized noble gas has increased the prospect for high-resolution MRI, especially in areas such as the lungs, organs not accessible to proton MRI because of their low water content. Its high degree of polarization more than makes up for its low density, increasing overall SNR and thereby improving image quality. And because the degree of polarization is independent of field strength (because polarization is not thermal), the external applied field need not be as strong as that for conventional MRI. Lower field strength reduces magnetic susceptibility difference inhomogeneities and could lead to lower instrument cost.

The two possible isotopes for this process, ^3He and ^{129}Xe , have different properties and merits. Advantages of ^3He over ^{129}Xe include the higher degree of polarization achievable, longer relaxation times in many environments [31], and better SNR because of its higher γ [31]. In our studies, however, Xe was used. Its relatively high melting point (161.4 K) allows it to be frozen at liquid nitrogen temperatures (LN_2 , bp 77K), allowing for the possibility of cryo-pumping. In addition, Xe is soluble in many liquids, making dissolved-state NMR spectroscopy feasible. In fact, others in our group have studied Xe dissolved in blood and identified resonances from gas, blood, and tissue phases [32]. Xenon is also lipophilic, suggesting that it may be able to accumulate in the myelinated, lipid-rich regions of the central nervous system. Accumulation of Xe in the brain could allow for brain imaging studies in the future.

In order to use hyperpolarized xenon (hypXe) to image human lungs, it must be produced in large enough quantities – on the order of liters. One member of the group, Dominik Hoffmann, has developed a portable, self-contained unit, mounted on a Rubbermaid[®] hand-cart, which contains all the equipment necessary to produce the polarized gas on the required scale. This human inhalation cart consists of (i) a large (644 cm^3) pump cell, (ii) the lasers and accompanying optics, and (iii) the gas supply and pump. The glass manifold was made of Pyrex[®] borosilicate,

relatively easy to glass-blow because of its low melting point. Once the hypXe is transferred to a suitable container and properly inhaled, the lung space can be imaged on a clinical magnet tuned to the ^{129}Xe resonance. Figure III.1 and III.2 shows views of the cart, and Figure III.3 shows a close view of the manifold and freeze cell.



Figure III.1. Front of human inhalation cart. Xe, N₂, and He cylinders are visible, as are the temperature and pressure gauges. The oven surrounding the pump cell (black casing on left side of cart) has been opened to provide a view of the pump cell. A small inhalation bag mated to the cart outlet is visible on the right side.



Figure III.2. Back of human inhalation cart. The fiber glass cable from the laser diode arrays is visible, as are the laser-guiding and polarizing optics.

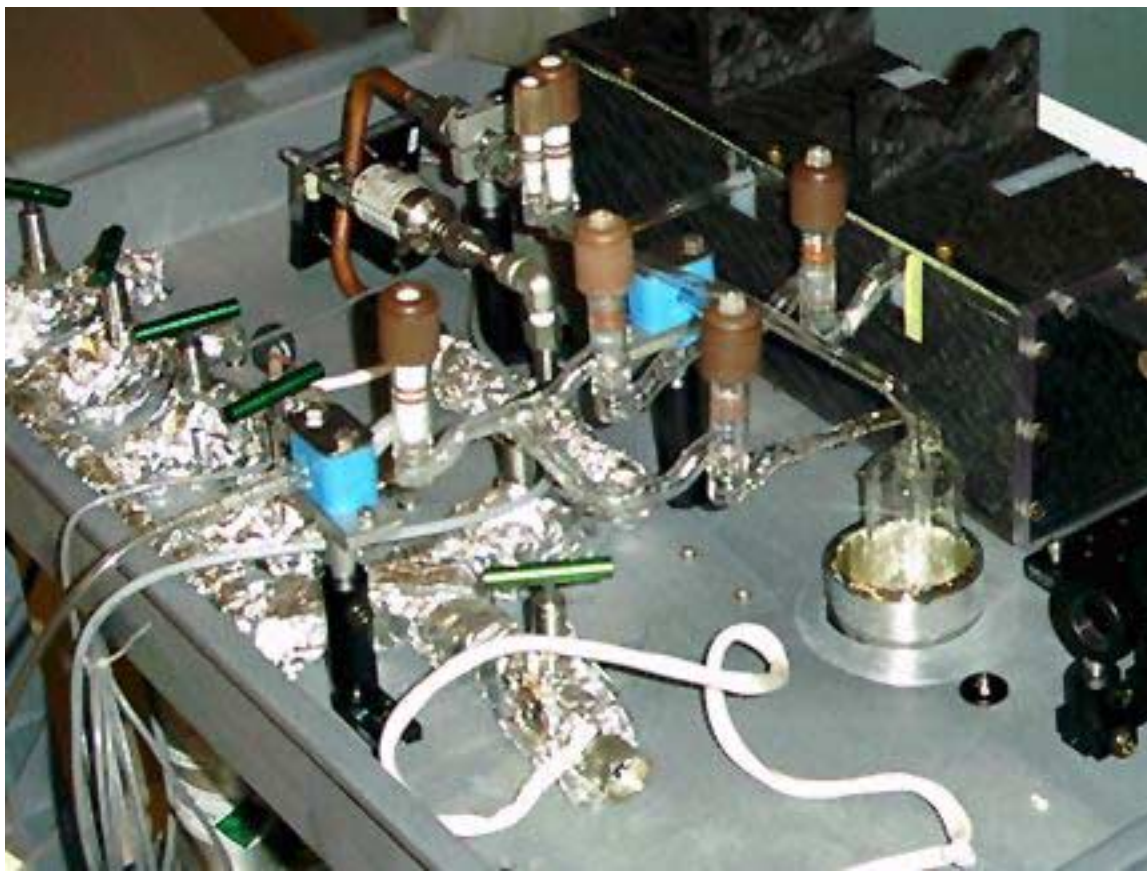


Figure III.3. Freeze cell and manifold of human inhalation cart. This close-up shows the metal and glass manifold, as well as the covered pump cell. The dewar surrounding the freeze cell is partially lowered to make the freeze cell visible.

Although O_2 was carefully excluded from the pump cell, Rb oxidation did take place over a long enough time scale (\sim weeks). Once oxidation reached deleterious levels, the Rb was replaced. This time-consuming labor involved fully oxidizing and washing out the Rb with water, a process that damaged the coating. Thus the coating had to be fully removed by washing and bathing the cell for one hour with “piranha solution”, an acidic mix of sulfuric acid and hydrogen peroxide [33]. The cell was then washed with a solution of OTS in hexanes, washed with acetone and ethanol, and baked at $\sim 200^\circ C$ and evacuated overnight. An ampule containing metallic Rb was then fused to the cell with a methane-oxygen torch, with care taken to avoid heating the cell excessively, which would destroy the coating. The Rb was then chased inside the cell by applying temperature gradients across the glass with a glass blowing torch, and the ampule was detached.

The optical pumping process was carried out in the fringe field of a 1.5 tesla (63.9 MHz) 60 cm bore IBM prototype NMR magnet with a Surrey Medical Imaging Systems (SMIS, Surrey, England) console at Brigham and Women's Hospital (BWH, Dept. of Radiology). The 63.9 MHz refers to the resonant frequency of ^1H ; for ^{129}Xe the operating frequency is 17.7 MHz. The manifold and pump cell were first evacuated to a few millitorr to remove impurities. An insulated air flow-through cartridge heater kept the pump cell at 130°C to produce adequate Rb vapor pressure. Once the temperature stabilized, the pump cell was filled with the proper mixture of Xe, N_2 , and ^4He (for typical pressures *vide infra*). The helium was present to increase the pressure in the cell; pressure-broadening of the Rb absorption line allows more laser power to be absorbed, since high-power diode laser arrays' power output has a significant spectral width. The helium in this case was ^4He , cheaper to obtain than ^3He (and ^3He would act as a polarization sink for ^{129}Xe polarization). For trial purposes natural abundance Xe (26% ^{129}Xe , \$12.50 per liter, Middlesex Gases and Technologies, Everett, MA) was used due to the higher cost of isotopically enriched Xe (90% ^{129}Xe , \$700 per liter at the time these experiments were performed; 78% ^{129}Xe , \$5500 per liter now).

Once the pump cell was valved off, the manifold was evacuated and the pumping laser was shined on the cell window. A fiber optic-coupled diode laser array (Optopower Corp., Tucson, AZ) provided ~ 15 watts of circularly polarized light at 795 nm (3 nm FWHM [34]). Since the Rb pumping rate and equilibrium polarization scales with incident laser power, an increase in laser power should increase Rb (and therefore Xe) polarization. Available laser power is one of the most important limitations to optical pumping. With this motivation a fiber optic system was implemented to coalesce the power of up to four lasers into one array. We hoped that we would see a proportional four-fold increase in polarization using this 4-into-1 light beam.

Once the Xe was sufficiently polarized it was removed from the pump cell by cryo-pumping. A dewar of LN_2 was placed around the freeze cell to create a cold trap. Once the rest of the manifold was valved off, the valve to the pump cell was opened and the gas mixture was allowed to slowly flow through the freeze cell via the flow-through glass line, with the vacuum

pump valve opened slightly to suck the gas through. Because of the relatively high freezing point of Xe, it froze onto the walls of the pump cell, forming a white snow-like coating. After waiting several minutes to allow all the Xe to solidify, the other gases were pumped away, leaving only the hypXe in the freeze cell. If this cell is properly coated, chilled, and kept in a uniform field, T_1 can reach several tens of hours [31]. A large evacuated Tedlar[®] gas sampling bag (Jensen Inert Products, Coral Spring, FL) was then mated to the manifold and the hypXe was thawed and allowed to flow into it. Other groups have chosen this particular bag because of the relatively long T_1 (~15 minutes) of Xe gas held within [35]. Gas would only flow into the bag until pressures were equalized; thus a residual volume of hypXe was left in the manifold. Care was taken to make sure there were no ferromagnetic materials nearby and the local field was fairly constant, to prevent destruction of polarization.

Because the pump cell was filled with one atmosphere of Xe, the bag, which was at atmospheric pressure, could also contain a maximum of the volume of the pump cell, or 644 ml. The actual amount was significantly less, however, because of residual gas in the manifold as well as losses during the freezing and thawing procedures. An average person's tidal lung volume is a few liters; hence it is possible to inhale essentially all the hypXe sample in the bag. The procedure for inhaling the gas was designed to maximize the signal while ensuring the safety of the human subject. A physician's presence was obtained to ensure proper treatment. The subject was to exhale completely to minimize the amount of O₂ present in the lungs. Then the hypXe would be inhaled for a reasonable breathhold duration. After experiments were performed, the patient would ventilate with air.

The first characteristic of the system we investigated was the dependence of hyperpolarization on pumping time. To measure polarization, we siphoned off a small volume of the gas mixture (8% of pump cell volume) into a transfer cell mated to the cart outlet receptacle. We then placed the transfer cell in the magnet and measured the NMR signal from a 90° pulse. By comparing the signal to that from a thermal Xe phantom (and correcting for pressure differences, etc.) we could calculate the polarization of the hypXe. To determine the dependence

on pump time we siphoned off samples at regular intervals during a pump-up. When taking continuous siphons in this manner we had to take into account the decreasing pressure (and therefore density) in the pump cell when calculating polarization.

An important parameter determining the degree of Xe polarization achievable was the T_1 of the pump cell. If its T_1 were short, due to impurities in the walls or improper coating, polarization would saturate at a lower level and rapidly diminish when the laser was turned off. In order to determine the pump cell's T_1 , we pumped for an hour and then cooled the cell with water. This cooling was vital, for with the laser turned off the Rb become a polarization sink rather than source. Cooling the cell decreased the Rb vapor pressure and reduced this effect. We then siphoned off gas samples and measured the decay of Xe polarization.

This process was carried out for all compartments in which the gas remained for a significant duration – the freeze cell and inhalation bag. Whereas most other experiments with the inhalation cart were performed using the 1.5 T 60-cm magnet, the inhalation bag T_1 experiment was carried out using the 4.7 T Omega, in order to take advantage of its better pick-up coils. The surface coil (wire loop) used with the 1.5 T was adequate for measuring the signal of small transfer cells, which fit within the coil. But the larger bag extended beyond the diameter of the coil; thus RF pulses did not tip all atoms equally. This defect would result in an increase in measured polarization, for spins at the periphery which were not tipped could subsequently diffuse towards the center and contribute to a falsely higher level of polarization. This error would manifest itself as a falsely longer T_1 . The solenoid coil used with the 4.7 T, on the other hand, enclosed the bag completely. T_1 was measured by repeatedly tipping the hypXe polarization into the transverse plane with a small known tip angle, and determining the polarization decay, given by the reduction of NMR signal as a function of time.

The non-renewable polarization of hypXe necessitates modification of the imaging sequence. A 90° RF pulse is no longer possible, for it would destroy all the polarization after the acquisition of only one line of k -space. Thus the 90° pulse in Figure II.4 must be replaced by a smaller flip-angle pulse. The sequence can be further modified by introducing a pair of gradients

to create a gradient echo. It is often hard to detect a FID immediately after an RF pulse because of the finite time required for the spectrometer to stop sending RF and start acquiring. The delayed gradient echo can be measured more accurately. Figure III.4 illustrates an imaging sequence with these modifications. One example of this kind of modified sequence is the fast low-angle shot (FLASH) [36].

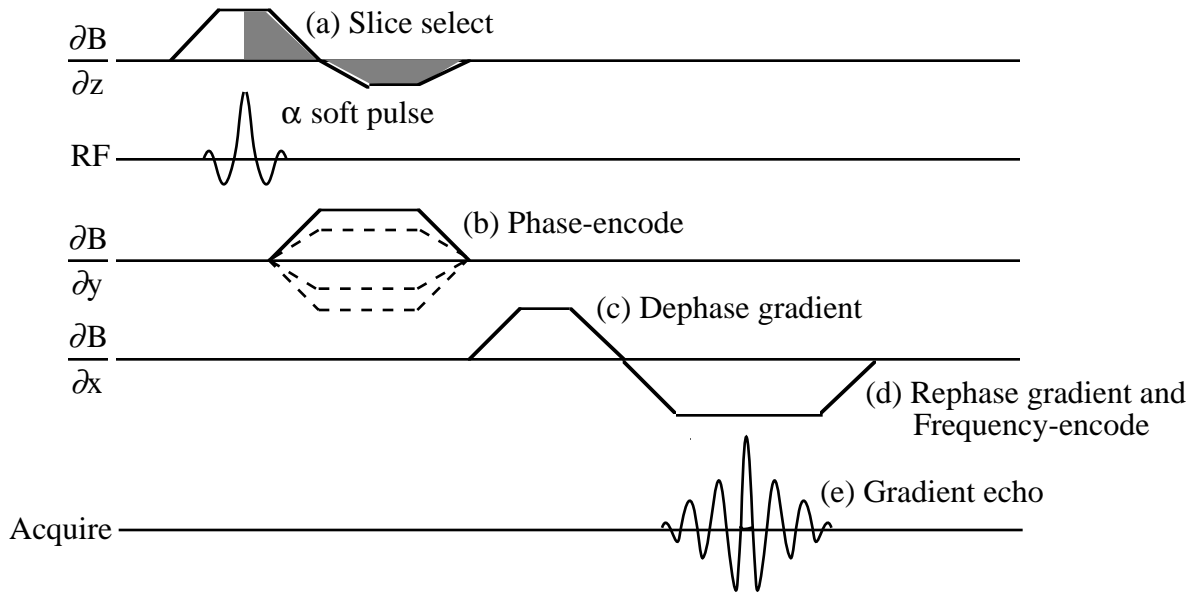


Figure III.4. Imaging sequence with low-angle pulse and gradient echo. (a) Slice select gradient during RF pulse limits excitation to a slice in the z direction. Small tip angle α conserves polarization. (b) Phase gradient encodes phase information. (c) Dephasing gradient manually decoheres spins. (d) Subsequent rephasing gradient refocuses spins, creating gradient echo. Gradient is kept on as read gradient, encoding frequency information. (e) Gradient echo is acquired.

III.2 Diffusion Measurements

Previous studies of time-dependent restricted diffusion have been limited to porous media filled with liquid such as water [37]. Using gases to study diffusion has several advantages over liquid: the higher diffusion rate allowing the study of a larger range of pore sizes, the reduced surface relaxation, and the ability to inhale gas for *in vivo* lung studies. The results presented below are the first instances of NMR used to measure time-dependent gas diffusion.

Gas diffusion measurements were carried out using a 4.7 T (200 MHz) horizontal bore NMR magnet. The magnet provided gradient strengths up to 7 G/cm and a minimum duration of 750 μ sec. The magnet was used with a GE Omega/CSI spectrometer operating at 55.3 MHz for ^{129}Xe .

All thermal Xe diffusion measurements were carried out in valved glass cells with a volume of 80 cm^3 , prepared by Mr. Charles Raworth of Wilbur Scientific. To enhance thermal Xe signal strength, measurements were performed using gas isotopically enriched to approximately 90% ^{129}Xe . A method was devised to recover the ^{129}Xe after experiments by freezing it into a storage bottle. For these thermal experiments, O_2 gas was added in order to reduce the T_1 of the Xe from several minutes to ~ 1 second. Because of the low polarization of thermal Xe, extensive signal averaging had to be performed to enhance the SNR, which increases as the square root of the number of averages. Averaging requires that the sample fully recover its polarization between spin echoes so that the signal is constant from echo to echo. For an exponential recovery, this requirement means waiting about five time constants, or T_1 periods, a delay called the repetition time T_r . Hence the necessity of the paramagnetic O_2 .

Experiments with hypXe were performed in 25 cm^3 coated cells with 3 atm natural abundance Xe. With hypXe, O_2 was carefully excluded to maintain the longest possible T_1 , since laser polarization is non-renewable. Nitrogen was excluded as well so that diffusion measurements of pure Xe could be obtained. Pumping for 30 minutes at 85 $^\circ\text{C}$ produced polarizations of approximately 1% - 4%, as compared to a value of $\sim 7\%$ reached in sealed cells with 50 - 100 torr N_2 . Thus the reduced polarization, some of which may have been due to the exclusion of N_2 , was not severe. In this case the Xe was optically pumped in the fringe field of the 4.7 T magnet.

The cells were filled using the cell filling station in our lab at the Harvard-Smithsonian Center for Astrophysics (CfA). The volume ratio of the manifold to the cell plus manifold was determined using an inert gas (usually N_2). The manifold was then filled with the appropriate amount of gas with the cell valve closed, and then the valve was opened, allowing the gas to enter the cell. The cell was bathed in LN_2 so that the Xe would freeze in; thus Xe was always filled first,

followed by O₂. In some experiments we also used the gas sulfur hexafluoride (SF₆) to decrease the rate of Xe diffusion. SF₆ is a large, relatively inert molecule which we hoped would slow diffusion enough to permit the study of small pore spaces, such as lung alveoli (~ 100 μm). The melting point of SF₆ is 222.45 K, allowing it to be frozen with LN₂ as well. The practical lower limit for δ , the magnetic field gradient duration, was 750 μsec with the 4.7 T magnet. For pure Xe at 1 atm, the free gas diffusion coefficient is $D_0 = 5.7 \times 10^{-6} \text{ m}^2 \text{ sec}^{-1}$, giving a diffusion length of ~ 65 μm during the minimum δ . From the above discussion of the narrow pulse approximation, we would need a diffusion length of order 14 μm to study 100 μm pores. Thus the diffusion length must be decreased by a factor of 5, corresponding to a 25-fold decrease in D_0 .

Before experiments were performed, the pick-up coil had to be tuned and the magnet shimmed. The coil was tuned with the cell inside to correct for any effects the cell contents had on tuning, called loading effects. For gas-filled cells, loading was minimal, but biological samples could load the coil significantly because of the presence of salts and other charged particles. The coil was placed in the middle of the magnet, where the field was the most homogeneous, and RF of varying frequency centered at 55.3 MHz was swept through the coil. A display showed the coil's resonance peak, which was adjusted such that it centered on 55.3 MHz by turning a variable capacitor on the coil. The width of the coil's resonance peak is a measure of the coil's *quality factor*, or Q , given by the operating frequency divided by the half-maximal width of the spectral peak (full-width half-max, FWHM). A coil's Q depends on physical characteristics such as evenness of wire wrapping and consistency of turn radius, as well as experiment-specific criteria such as operating frequency, loading, etc. The coil used for gas measurements was home made and had an unloaded Q of ~ 280.

Once the coil was tuned the magnet was shimmed, or made homogeneous. Electric current through several sets of shimming coils could be adjusted to increase the homogeneity of the field at the center of the magnet. A programmed routine cycled through user-assigned sets of shim coils searching for an optimal setting. The final preparatory step was the determination of RF power and duration necessary to produce a 90° pulse. From [1.9] we know that the tip angle

θ depends on RF pulse strength and duration. The pulse duration was varied until the FID disappeared, corresponding to a 180° pulse. Halving the duration would then produce a 90° pulse. This technique was better than directly looking for a 90° pulse because of the relative ease of determining an absence of FID signal over determining its maximum.

For studies of free diffusion, all three sequences described above were used to establish consistency [38]: the standard PGSE sequence described in Figure II.6, the stimulated echo sequence (PGSTE) in Figure II.7, and the bipolar gradient pulse PGSTE sequence depicted in Figure II.8 with $n = 2$. In heterogeneous media, the bipolar sequence was used to compensate for the large background gradients present at the gas-solid interface. Eight to sixteen averages was typical for free diffusion studies, and thirty-two to sixty-four for time-dependent (restricted) diffusion.

Special consideration was given to experiments with laser polarized gas; excitation with a 90° pulse was not repeatable because of its non-renewable polarization. Thus the sequences described above would not be useful. Members of our group and collaborators have modified imaging sequences by using a small flip angle so as not to deplete polarization [39]. They have also taken into account the fact that a constant low flip angle will result in varying signal strength, since the component in the transverse plane will decrease successively. One can compensate for this effect by increasing the flip angle each time, thus maintaining constant signal strength. But even these sequences suffer systematic problems such as errors from non-uniform 180° pulses.

Instead, other members from our group designed two pulse sequences which they called pulsed gradient echo (PGE) and Multiple-PGSE (MPGSE) [38]. PGE is very similar to PGSE, the differences being the variable flip angle and the lack of the problematic 180° pulse. By keeping the diffusion time gap between the gradients, this sequence preserves the ability to study time-dependent diffusion. Others [40], [41], [42] have used similar techniques, but without this gap between the pulses. Thus these previous techniques employed essentially a constant-gradient sequence which can not be used to study time-dependent diffusion. The PGE sequence is shown in Figure III.5

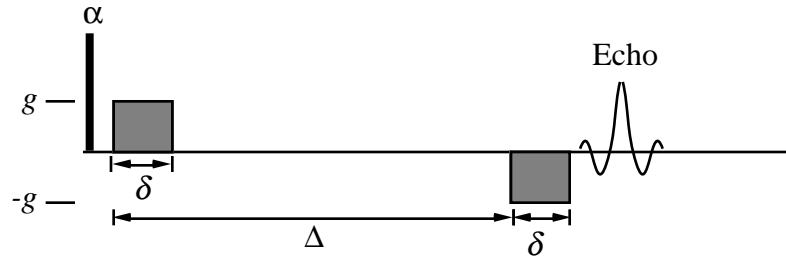


Figure III.5. Pulsed gradient echo (PGE). The low flip angle α conserves polarization, and the lack of a 180° pulse removes inconsistency problems.

The PGE sequence, however, is limited by the fast T_2^* relaxation of polarization in the transverse plane in heterogeneous systems (porous media, etc.). The MPGSE technique (Figure III.6) solved this problem by constantly refocusing the echoes. A single excitation brings all the polarization into the transverse plane, in which pairs of opposing gradients create a train of spin echoes. These gradient pairs are separated by 180° pulses to refocus the spins. Small clean-up gradients in a direction orthogonal to the encoding gradients were used to remove irregularities from the 180° pulses. The MPGSE suffers from signal loss due to T_2 decay, which, while longer than T_2^* , still limits its usefulness for longer diffusion times, particularly in heterogeneous systems. A stimulated echo pulse sequence is necessary to overcome this limitation by applying a 90° pulse to lift the polarization out of the transverse plane where it can be depleted by T_2 effects. Such a sequence has been developed and will be useful for future study [43].

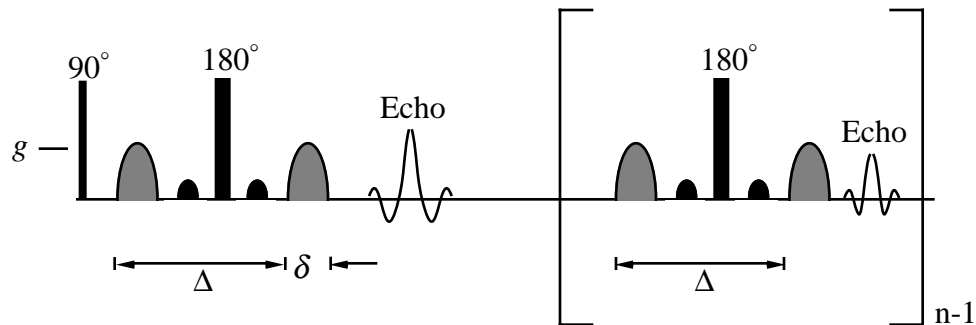


Figure III.6. Multiple pulsed gradient spin echo (MPGSE). All spins are excited by the 90° pulse and constantly refocused by pairs of phase-encoding gradients separated by 180° pulses since polarization is non-renewable. Small gradients (shown in black) on either side of 180° pulses remove irregularities. Echo attenuation provides a measure of spin diffusivity.

For studies of the rat lung we used the 4.7 T magnet with the solenoid pick-up coil. We used a gas mixture of Xe / O₂ = 0.67 atm / 0.33 atm (henceforth, “test gas”), for a total of one atmosphere pressure. One of the long-term goals for studying diffusion in the rat lung was to test the ability to measure alveolar microgeometry. Given the complexity of dealing with an animal specimen, our experiments with the rat were preliminary attempts to detect a low-pressure thermal Xe NMR resonance and learn about relaxation rates in the lung.

Previously sacrificed rats were obtained from the Harvard School of Public Health. Dr. George Topulos prepared the rats for the experiments by exposing the rats’ trachea and suturing a small catheter into the airway. The gas was filled in 60 ml syringes (Becton-Dickinson, Franklin Lakes, NJ) fitted with LuerLok[®] receptacles. These receptacles were found to be fairly airtight; the mildly leaky trachea-catheter interface was sealed with Krazy Glue[®].

A 3-way stopcock on the tubing attached to the trachea allowed for the connection of a filling syringe and a pressure-controlling apparatus. The filling syringe was used to flush and inflate the lungs with test gas. Because we will eventually be interested in measuring microstructure at various lung volumes, we designed an apparatus that would allow us to control the pressure in the rat lung. This constant pressure apparatus was simply a tank of water with a ruler marking vertical distance. An open syringe connected to the stopcock with tubing and submerged in the water acted as a pressure control. By keeping the whole system filled with gas and varying the height of the syringe in the water we could control the pressure inflating the rat lung. We were able to determine how much gas was leaking by observing the gas level in this “pressure gauge”. There was minimal leakage (on the order of a few mls per hour), which was compensated for by constantly bubbling test gas into the open end of the syringe gauge from a test gas reservoir. Our test gas reservoir was a 500 cm³ stainless steel cylinder filled to capacity with 350 psi test gas (12,074 torr natural abundance thermal Xe and 6,037 torr O₂). It was filled in the same manner as the glass cells on the cell-filling station at the CfA. The total lung capacity (TLC) of an average young 160 gram rat is ~ 6 ml, corresponding to an airway pressure of 30 cm H₂O.

The functional residual capacity (FRC) during relaxed breathing is ~ 2 ml, corresponding to 2 cm H₂O airway pressure [44].

Once the rat was placed in the solenoid coil, the gas-filled syringe was attached and the rat lung was ventilated ten times with five ml test gas, with passive exhalation into the room. This ventilation diluted and removed other gases, and assured that the lungs were filled with test gas. After the coil was tuned and the magnet shimmed experiments could begin.

IV RESULTS AND DISCUSSION

IV.1 Large-scale Polarization of Xe for Human MRI

Using a 25 cm³ cell we were able to achieve near theoretical levels of polarization – up to 7% – with a 30 minute pump-up time. Applying that success to the inhalation cart, however, proved to be non-trivial. The 26-fold volume increase introduced questions about Rb vapor homogeneity, degree of laser absorption, optimal temperature and gas partial pressures, etc. We found maximal polarization using 100 torr N₂, 2 atm ⁴He, and 1 atm Xe at a cell temperature of 130 °C. Figure IV.1 illustrates a typical pump-up curve, showing both raw and pressure-corrected polarization.

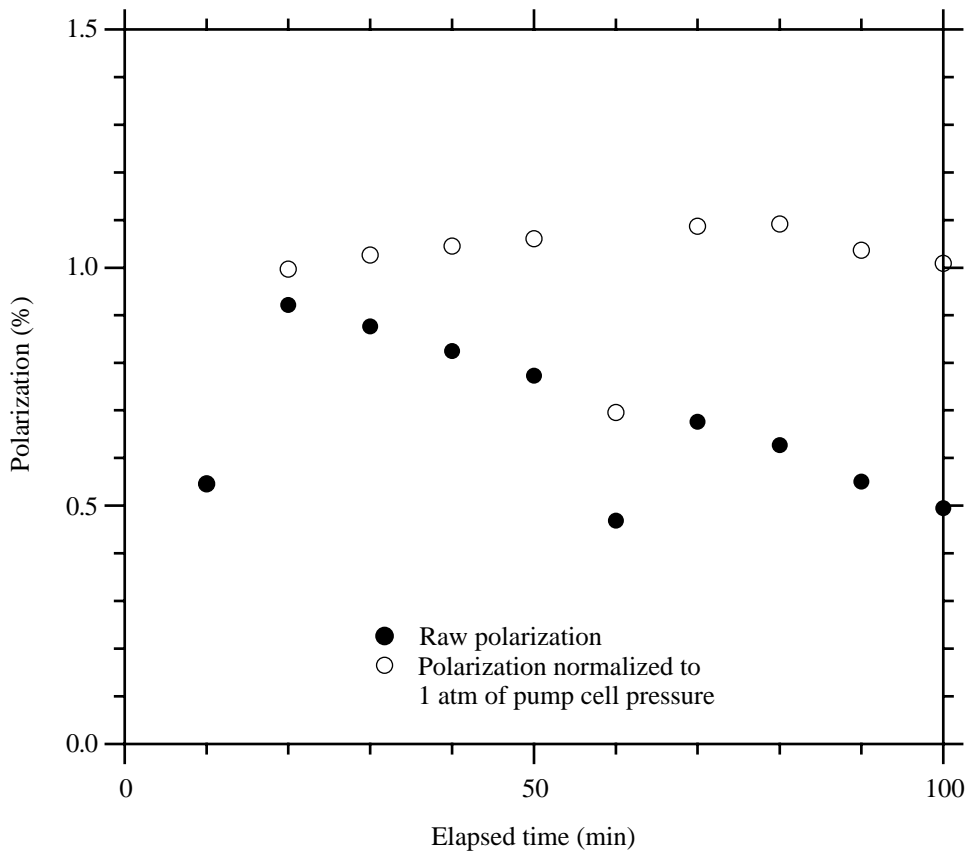


Figure IV.1. Typical pump-up curve. Pump cell polarization vs. elapsed pumping time is shown.

The first data point (10 mins) did not need to be corrected for pressure, so the two symbols overlap (filled and open circles). The polarization value at 60 mins reflects an error in timing, not a true measurement. Under these conditions, we were able to produce $644 \text{ cm}^3\text{-atm}$ of $\sim 1\%$ polarized Xe. The actual polarization varied due to differences in Rb oxidation and cell coating.

In order to increase polarization, we tested the efficacy of using the fiber optically coupled (4-into-1) laser array. Because one laser was being repaired, the cell was pumped up with each of three lasers individually, and a polarization of $\sim 1\%$ was measured in all three cases. When the three were coupled, however, the polarization actually decreased rather than increasing by 3-fold. We suspect a technical problem due to excess heating of the pump cell thermister. If the laser were selectively heating the thermister rather than heating the entire cell uniformly, the thermister would detect a temperature higher than the actual temperature in the pump cell. This would prematurely lower heating output and thus keep the cell too cold, preventing the formation of adequate Rb vapor density. We plan to investigate further by tuning the laser off resonance, but with the same power output, to determine whether this overheating effect is relevant.

In order to make sure we were not losing polarization due to short relaxation times, we measured the T_1 of the pump cell, freeze cell, and inhalation bag. Figure IV.2 shows a typical T_1 time for the pump cell. Again, the raw polarization was corrected for decreasing pump cell pressure. The measured value of 85 minutes is long compared to the time between shutting off of the laser and freezing in the freeze cell, lending credibility to the efficacy of coating.

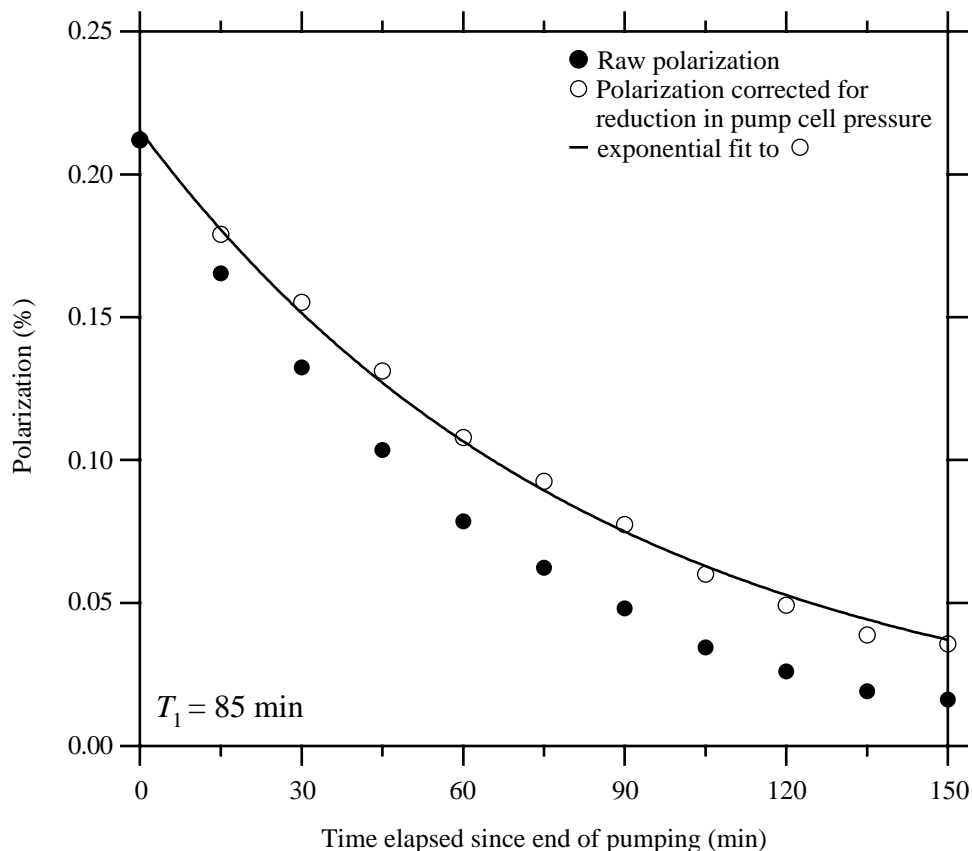


Figure IV.2. Typical T_1 for pump cell. Measured value of 85 minutes lends assurance that we are not losing polarization to T_1 decay.

We investigated the T_1 of the freeze cell as well, for it usually holds the hypXe for the longest time. After pumping up a sample, we froze the gas into the freeze cell and siphoned small volumes. Our results are shown in Figure IV.3. Again, the measured value of 75 minutes should provide adequate time to harvest the hypXe into the inhalation bag. Since the transit time in the glass manifold was small (a few seconds), we were less concerned with its T_1 ; moreover, since the pump cell, freeze cell, and manifold were coated simultaneously, we would have no reason to suspect inadequate manifold coating.

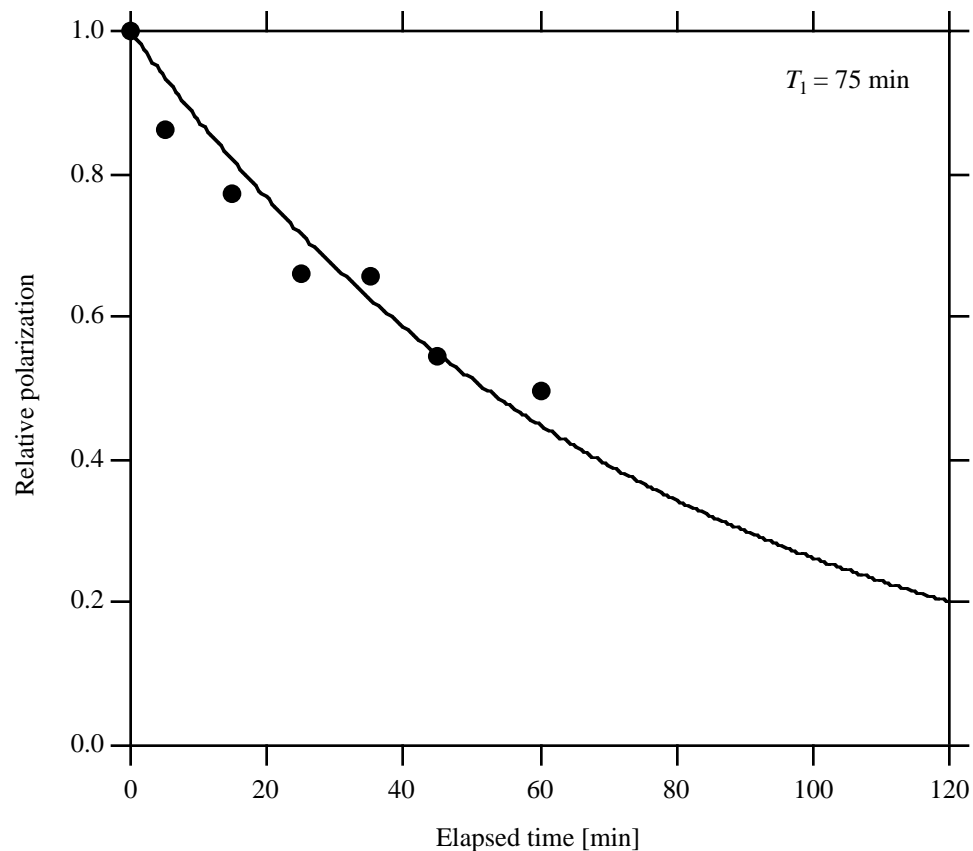


Figure IV.3. Typical T_1 for freeze cell. Measured value of 75 minutes is consistent with 85 minute T_1 of pump cell.

The last of our T_1 measurements involved the inhalation bag. We thawed some hypXe into the bag and placed it in the 4.7 T NMR magnet. Using a tip angle of 18° and correcting for decay due to tipping we measured a T_1 of 14.7 minutes, similar to the value of 15 minutes determined by others [35] (Figure IV.4):

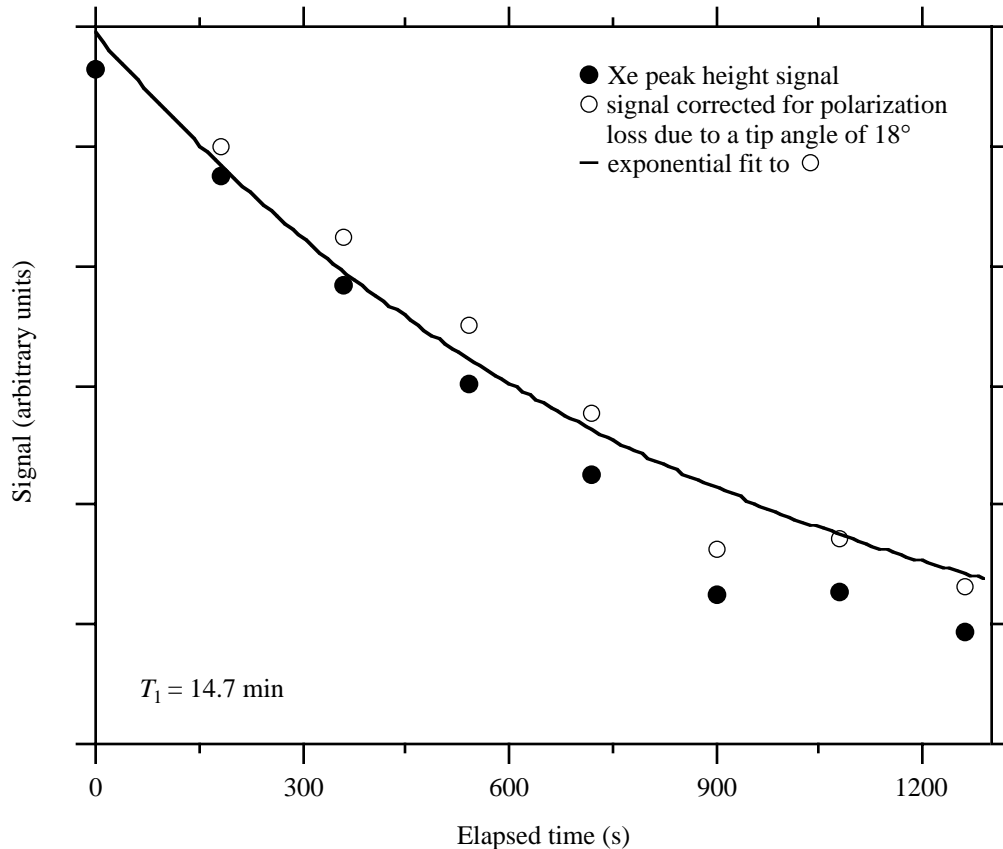


Figure IV.4. Typical T_1 for inhalation bag. Measured value of 14.7 minutes is consistent with previously published results and long enough to allow human inhalation without serious loss of polarization.

We used a FLASH sequence to image the inhalation bag. Using a flip angle of 10° and a 65×130 resolution we obtained this image (Figure IV.5). The line down the middle of the image is an artifact of the DC offset. If there is a DC offset on the RF pulse, it will appear on the NMR spectrum as a peak at zero frequency. For applications requiring signal averaging (as is the case with ^1H or thermal ^{129}Xe NMR), the RF pulse is given a different phase during each repetition so that the sum of the phases cancels, eliminating this DC offset peak. This process is called phase cycling. Since we were using hypXe, we did not need to signal average, and thus could not employ phase cycling to remove the DC offset.

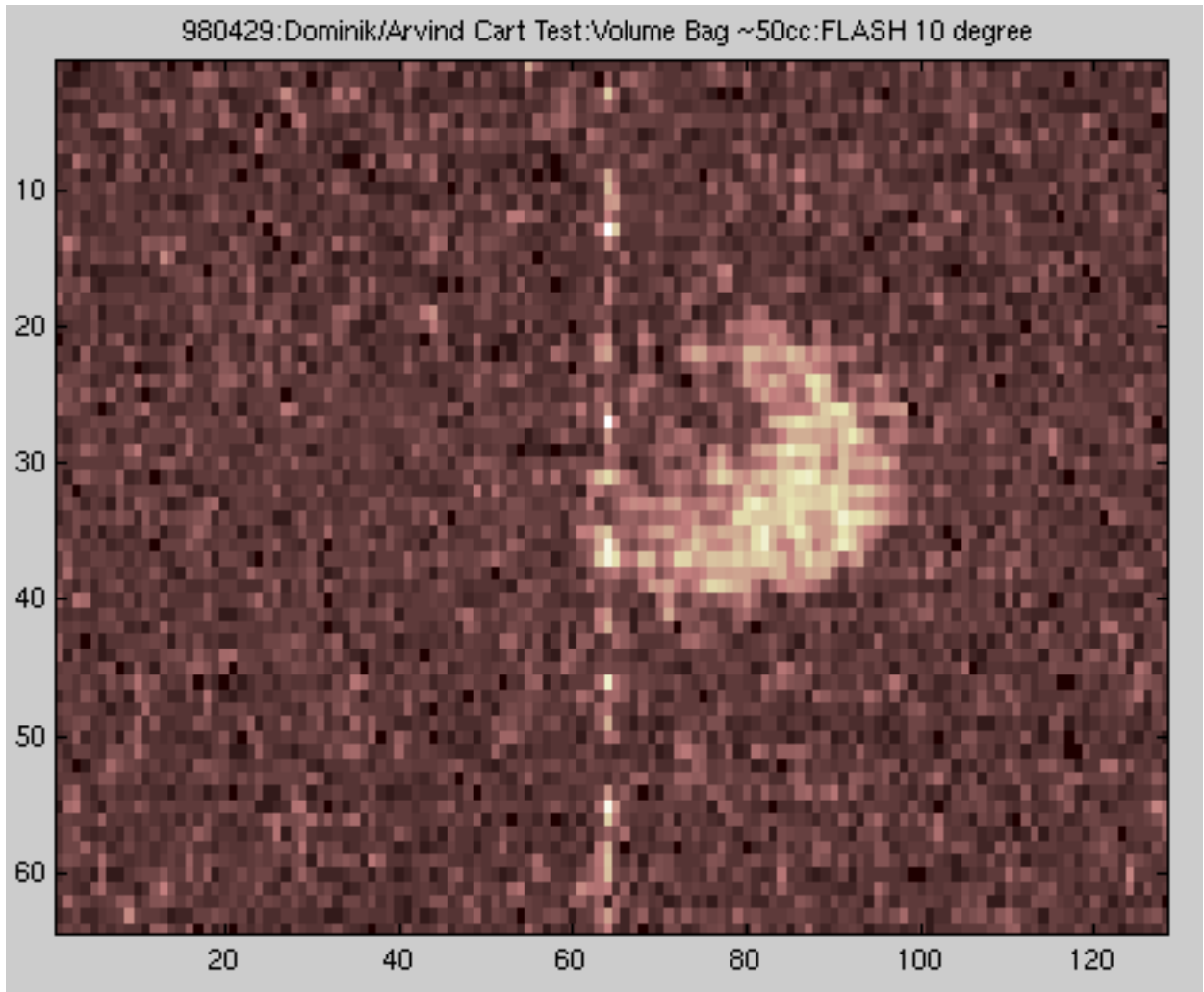


Figure IV.5. Image of inhalation bag. FLASH sequence was used with 10° tip angle to compensate for loss of non-renewable polarization. Resolution is 65×130 .

We plan to move the inhalation cart to the clinical magnet and begin imaging experiments using the hypXe produced by the cart. We hope to demonstrate the ability to polarize gas in the more restrictive clinical setting, harvest it through the freeze-thaw process without losing significant polarization, and generate human lung images.

IV.2 Diffusion Results

We report results from four series of experiments with gas filled glass cells, and one performed in a rat lung. The first set of experiments [38] involved the study of free diffusion using thermal Xe with (i) the standard PGSE (Figure II.6), (ii) a PGSTE variant (Figure II.7), and (iii) the bipolar PGSTE sequence with $n = 2$ (Figure II.8). Their consistency in measuring D showed the efficacy of using such pulse sequences to study free gas diffusion. The second set of results involved the study of restricted diffusion using thermal Xe with the bipolar gradient to compensate for background magnetic field gradients due to local magnetic susceptibility variations. The porosity of the glass bead-packed cells was calculated following the logic outlined above and matched previous results. The new PGE and MPGSE sequences were applied to the study of free diffusion using laser-polarized hypXe in the third experimental set and shown to match results using thermal Xe. These three groups of experiments were chiefly conducted by Ross Mair, a post-doc in the group. The fourth set of experiments was conducted with SF₆ added to determine its effect on the diffusion rate of Xe. We report a slight decrease in the Xe diffusion rate in the presence of SF₆, but not the order-of-magnitude decrease desired to probe length scales of ~ 100 μm . Finally, we began to apply the diffusion measurement techniques to study the lung space of a rat. Despite low thermal polarization and gas pressure (~ 1 atm), we were able to detect a Xe NMR signal from the rat lungs and roughly measure its T_1 and T_2^* .

IV.2.1 Studies of thermal Xe free diffusion

Glass cells were filled with 3 atm enriched Xe and 2 atm O₂ to decrease T_1 . Diffusion was measured using all three sequences (PGSE, PGSTE, and PGSTE with bipolar gradients). The diffusion times Δ covered a wide range, from 75 - 1000 msec, and δ for the half-sine-shaped gradient pulses was kept constant at 2.4 msec for PGSE and PGSTE, and 1.2 msec for each of the two gradient pulses in the bipolar PGSTE, adding up to the same 2.4 msec. All three methods yielded the same diffusion coefficient, establishing the consistency of all three methods and

robustness over a range of diffusion times. Since we were studying free diffusion, the measured diffusivity did not depend on allowed diffusion time, as expected. The average value of D for 3 atm Xe in 2 atm O_2 was $1.37 \times 10^{-6} \text{ m}^2\text{sec}^{-1}$. The standard deviation of this value, as well as all other reported values, is 3% or less. Errors are attributed to instrumentation limitations, curve-fitting uncertainties, etc.

To account for the presence of oxygen, the diffusion constant was measured for different pressures of O_2 , from 1 - 3 atm. The extrapolated value for 3 atm Xe without O_2 was $1.90 \times 10^{-6} \text{ m}^2\text{sec}^{-1}$. The diffusion rate scales inversely with pressure (eqs. [5.5] and [5.7]); hence the diffusion constant for 1 atm Xe is $D_{Xe-Xe} = 5.71 \times 10^{-6} \text{ m}^2\text{sec}^{-1}$, which agrees very well with previously published results using methods other than NMR [45], [46].

In order to obtain the rate of Xe diffusion in O_2 , similar experiments were performed measuring the diffusion constant with 2 atm O_2 and varying the Xe partial pressure. The measured Xe in 2 atm O_2 rate was $6.77 \times 10^{-6} \text{ m}^2\text{sec}^{-1}$, apparently not reported elsewhere. Thus $D_{Xe-O_2} = 13.5 \times 10^{-6} \text{ m}^2\text{sec}^{-1}$.

IV.2.2 Studies of thermal Xe restricted diffusion

Separate glass cells were packed with 2 and 4 mm glass beads (Dow Chemical, NY) and filled with 3 atm enriched Xe and 2 atm O_2 . The diffusion constant $D(t)$, now a function of diffusion time, was measured over a range of Δ from 12.5 - 1000 msec using the bipolar gradient PGSTE with δ as above. The diffusion rate behaved as expected: the initial rate was equal to that of free diffusion ($D(0^+) = 1.27 \times 10^{-6} \text{ m}^2\text{sec}^{-1}$), and it decayed with an initial slope proportional to the S/V ratio of the pores (interstitial space between beads) as per equation [5.3]. The data are shown in Figure IV.6 with normalized diffusion length (bead diameters) on the x - axis to facilitate comparison between the 4 and 2 mm diameter beads. These values were calculated by converting allowed diffusion time to diffusion length via [5.2] and the fact that $D_0 = 1.27 \times 10^{-6}$

$\text{m}^2\text{sec}^{-1}$ for 3 atm Xe in 2 atm O_2 . These lengths were then expressed as fractions of bead diameter.

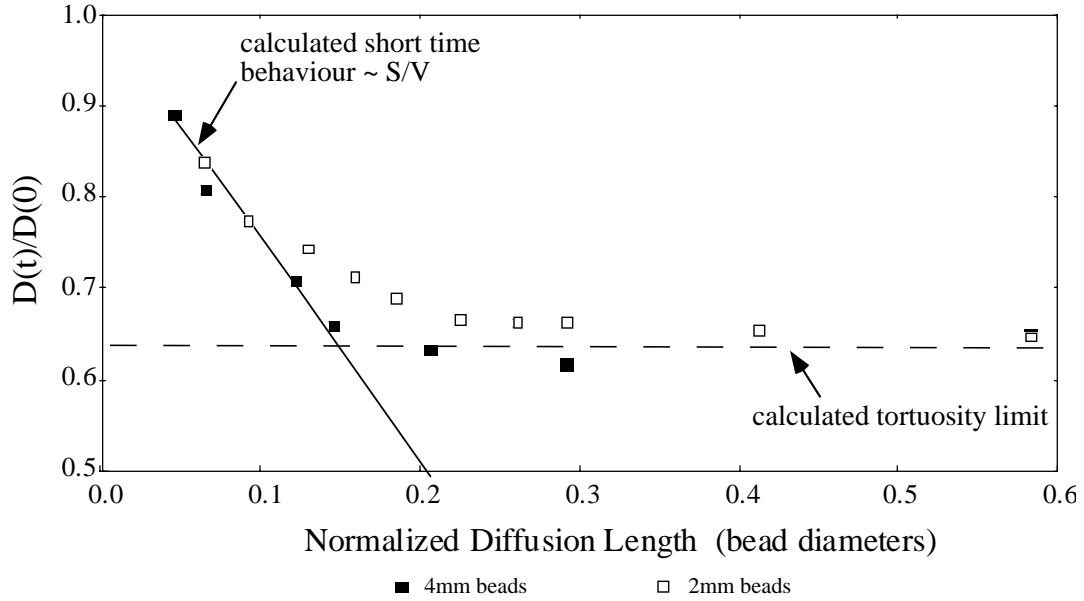


Figure IV.6. Time-dependent (restricted) diffusion curve for 4 and 2 mm beads. Values on the x – axis are normalized to diffusion lengths and expressed as bead diameters for comparison. Initial rate of change is proportional to S/V ratio of pores (solid line is theoretical value). Asymptotic value is related to porosity.

From the asymptotic behavior of $D(t)$, we have a measure of the porosity, $\phi^{1/2} = 0.64$, consistent with previous studies done with water-filled porous media [26]. This value is also consistent with a measured value of $\phi = 0.38$ for bead-packed cells [47]. For packed monosized spheres, it can be shown that $S / V = 6(1 - \phi) / d\phi$, where d is the bead diameter [47]. Thus for packed spherical beads with $\phi = 0.38$ the dependence of S / V on d is $S / V = 9.79 / d$. This theoretical line is plotted in Figure IV.6. As can be seen, the line matches the 4 mm bead data quite well, and passes through the earliest points of the 2 mm bead data as well. Thus the bipolar gradient PGSTE sequence was successfully able to reduce the effect of background gradients and measure restricted diffusion in the heterogeneous packed bead cells. Further studies will include extending the restricted diffusion curve for these and other bead sizes to longer diffusion times.

The success of this sequence is promising in view of applying this method to studying the microstructure of human lungs.

IV.2.3 Studies of laser polarized Xe free diffusion

In order to use the new PGE and MPGSE sequences to study the hypXe, the techniques first had to be evaluated. Thus they were tested on a sample of thermal Xe (3 atm enriched Xe, 2 atm O₂) and found to yield free diffusion values nearly identical to that determined by the other techniques. Using the PGE sequence with hypXe and diffusion times of 50 and 100 msec yielded diffusion coefficients of $1.90 \times 10^{-6} \text{ m}^2\text{sec}^{-1}$ and $1.91 \times 10^{-6} \text{ m}^2\text{sec}^{-1}$, again in agreement with data presented above for 3 atm Xe (without O₂). Using the MPGSE sequence, a longer diffusion time could be studied since the constantly refocusing gradients eliminated T_2^* decay. Diffusion times of up to 500 msec were studied, yielding an average diffusion time of $1.89 \times 10^{-6} \text{ m}^2\text{sec}^{-1}$, again consistent with other experiments. Thus both new techniques were able to accurately measure free diffusion. The future ability to use these sequences to study restricted diffusion with hypXe would be an excellent tool for *in vivo* studies.

IV.2.4 Studies of thermal Xe free diffusion in the presence of SF₆

Sulfur hexafluoride was added to the Xe / O₂ cells in hopes of reducing Xe diffusivity to enable studies of small pores, including lung alveoli (~ 100 μm). Cells were filled with two combinations of the three gases. Two cells were filled with 2 atm natural abundance thermal Xe and 2 atm O₂. The amount of SF₆ was varied – 1 atm in one cell and 2 in the other.

We used the standard PGSE sequence with a diffusion time Δ of 50 msec, a gradient pulse time δ of 2.5 msec, a repetition time T_r of 8 sec, and 8 averages. The T_r was decided after a rough estimate of T_1 was made using the inversion-recovery method, in which the signal was seen to level off at ~ 8 seconds. A more precise T_1 analysis was performed subsequently using the inversion-recovery method. We also measured the T_2 relaxation time for both samples using the

CPMG method. Average measured diffusivities were $1.38 \times 10^{-6} \text{ m}^2\text{sec}^{-1}$ for the Xe/O₂/SF₆ = 2/2/1 cell and $1.10 \times 10^{-6} \text{ m}^2\text{sec}^{-1}$ for the Xe/O₂/SF₆ = 2/2/2 cell. Knowing D_{Xe-O_2} ($13.5 \times 10^{-6} \text{ m}^2\text{sec}^{-1}$) and D_{Xe-Xe} ($5.71 \times 10^{-6} \text{ m}^2\text{sec}^{-1}$) we calculated the diffusion rate of Xe in SF₆, D_{Xe-SF_6} . This result is shown normalized to 1 atm SF₆, along with a summary of the relaxation data, in Table IV.1 below.

Xe/O ₂ /SF ₆ (atm)	D_{Xe} (m ² sec ⁻¹)	T_1 (sec)	T_2 (msec)	D_{Xe-SF_6} (m ² sec ⁻¹)
2 / 2 / 0	1.85×10^{-6}	1.40	508	–
2 / 2 / 1	1.38×10^{-6}	1.43	335	4.43×10^{-6}
2 / 2 / 2	1.10×10^{-6}	1.41	263	4.88×10^{-6}

Table IV.1. Effect of SF₆ on Xe diffusivity. Measured T_1 , T_2 , and diffusivity are shown, as well as calculated Xe-in-SF₆ diffusion rate. Data with the same Xe and O₂ content without SF₆ are also given for comparison.

The T_1 rate did not change between the 2/2/0, 2/2/1, and 2/2/2 cells since the O₂ partial pressure was constant and SF₆ apparently causes minimal Xe depolarization (it is not paramagnetic). Unfortunately, the value for D_{Xe-SF_6} is not much smaller than D_{Xe-Xe} , suggesting that replacing Xe with SF₆ will not significantly reduce the rate of Xe diffusion. Increasing pressure would decrease diffusivity ([5.7]), but since we cannot inflate lungs with much more than one atmosphere of total gas *in vivo* that method will not work. Moreover, addition of SF₆ seems to reduce T_2 , complicating diffusion measurements and shortening their range of usefulness. Its inability to significantly reduce the diffusion coefficient, along with its shortening of T_2 , suggest that SF₆ is not suitable for our purpose. We are thus continuing our search for molecules with very large cross-sections for Xe scattering.

As discussed above, the diffusion length of 1 atm pure Xe during a 750 μsec gradient pulse is about 65 μm. Thus according to the narrow pulse approximation, the minimum length scale that could be studied using NMR measurement of time-dependent diffusion is ~ 400 μm. Although this will not provide resolution on the order of normal lung alveoli (~ 100 μm), it may still yield

interesting information about pathological lungs in which the pore space is larger than normal, as well as the microstructure of bronchioles. The eventual identification of a suitable gas to slow down Xe diffusion could increase this resolution further.

IV.2.5 Studies of diffusion in rat lung

Due to the inefficacy of SF₆ in decreasing the diffusion rate, we performed initial rat lung experiments with only Xe and O₂. Before running experiments in the rat, we wanted to characterize the test gas to determine its T_1 , T_2 , and diffusivity. Using the inversion-recovery and CPMG methods, as well as PGSE to measure diffusion, we obtained results shown in Table IV.2.

Xe/O ₂ (atm)	D_{Xe} (m ² sec ⁻¹)	T_1 (sec)	T_2 (msec)
0.67 / 0.33	6.92×10^{-6}	6.81	356

Table IV.2. Characterization of rat experiment test gas mixture. Measured values of T_1 , T_2 , and diffusivity are shown.

The calculated value for D_{Xe} using the above method gives 7.10×10^{-6} m²sec⁻¹, only a 3% deviance from the measured value. The long T_1 and low pressure mean signal averaging will take a substantial amount of time. Enhanced abundance Xe or hypXe will be necessary to overcome this problem.

We then inflated a rat's lung with the test gas mixture to measure these values in the animal. The rat weighed about 250 g and had been sacrificed about three hours prior to the experiments. Tests were performed at a lung pressure of 20 cm water (or 15 mmHg), as determined by the height of the syringe pressure gauge. We performed two experiments to detect a signal, with varying averaging parameters, and were successful in detecting the Xe resonance. The data are summarized in Table IV.3.

Tip Angle θ	T_r (sec)	Num. Averages	FWHM (Hz)	SNR
90°	3	512	209	~ 3
27°	0.75	2048	201	~ 3

Table IV.3. Xe resonance in rat lung. Data are shown from experiments to detect a signal from rat lung with differing tip angle (θ), relaxation time (T_r), and number of averages.

According to [1.12], signal strength is affected by tip angle θ and repetition time T_r . With a tip angle of 90° , we had to wait a relatively long time for polarization to rebuild between successive averaging scans. We did not know T_1 exactly, and guessed a T_r of 3 seconds would be adequate. Using a smaller tip angle of 27° we could reduce the T_r , compensating for the reduced signal by averaging over more scans. In this way we tried to optimize signal strength by varying θ , T_r , and the number of averages.

We performed a saturation-recovery experiment to measure T_1 , but we did not detect any signal during the experiment. We suspect the possibility of corruption of the experiment due to insetting *rigor mortis*, since by then several hours had passed since the rat was sacrificed. We can, however, get a rough estimate of T_1 from the above data. Again from [1.12], the initial signal strength is proportional to $\sin(\theta) \cos(\omega t) (1 - \exp(-T_r/T_1))$, and since the signal detected was approximately equal for both trials, we may set the corresponding factors for both experiments equal to each other and solve for T_1 . The value we calculate is ~ 1 second, a reasonable number given the T_1 of 6.81 seconds for the test gas in a syringe. We expect the T_1 in the rat lung to be slightly reduced due to the possible presence of contaminants in tissue. This is by no means a robust way of calculating T_1 , especially with only two data points and such low SNR, but it does serve as a rough indicator.

Due to the limited availability of magnet time we did not perform an experiment to measure T_2 , but we can get an idea of its value by looking at the width of the spectral ^{129}Xe resonance line, which provides information about T_2^* . The shorter T_2^* (and therefore the faster the FID decay), the broader the spectral line, since the time constant of FID decay scales inversely

with spectral linewidth. It can be shown that $\pi T_2^* = 1/\text{FWHM}$ [10]. The values from Table IV.3 slightly overstate FWHM. An instrumental exponential filter was present during the FID which added 50 Hz linewidth to the observed spectral line. Thus with a linewidth of about 150 Hz, we estimate a T_2^* of ~ 2.1 msec. Again, because of the low SNR caution is required when using this method. Nevertheless, it gives us an estimate of T_2^* , which is much smaller than the measured value of 356 msec T_2 relaxation in the isolated test gas. It is apparent that the heterogeneous character of the rat's lung is giving rise to susceptibility variations between the gas and tissue phase which cause deleterious background gradients. As expected, we will have to use the bipolar PGSTE gradient to compensate for these destructive background fields. In addition, the independence of hypXe polarization on field strength can be used to increase T_2 . Since T_2 scales as the inverse-square of the magnetic field [48], performing the experiment at 1.5 T instead of 4.7 T should increase our T_2 by a factor of ~ 10 .

We plan to proceed via a two-fold path. One avenue of further research will involve the search for a buffer gas with a very large cross-section for Xe scattering to reduce Xe diffusivity. If such a molecule can be found, we will continue our studies of lung space using restricted diffusion methods. In order to combat the problem of low SNR, we plan to start using either enriched thermal Xe or laser polarized Xe.

The other project under consideration is determination of S/V in lung alveoli by measuring the rate of Xe absorption into cellular tissue. Because the rate of Xe absorbance is proportional to the S/V of the air spaces and exchange surface, measuring this rate will provide an assessment of alveolar S/V . Others in our group have detected three resonance peaks from inhaled dissolved-phase Xe, putatively ascribed to Xe dissolved in blood plasma, red blood cells, and pulmonary tissue [32]. These three peaks are closely spaced and centered 200 ppm from the gaseous Xe resonance. We plan to study the time evolution of these dissolved Xe peaks immediately following the inspiration of a bolus of polarized Xe to provide a measure of alveolar S/V .

V CONCLUSION

The human inhalation cart has been fully characterized and tested, and is now ready for inhalation experiments. Its satisfactory T_1 and reproducible polarization output warrant its testing with the clinical magnet and MRI console. We hope to be able to obtain MR images of hypXe inhaled into the lung space of humans in the near future. Such images, which are not attainable by conventional MRI, could complement conventional chest MRI images to give a complete view of the human thorax. In addition, hypXe lung images could be used in conjunction with blood perfusion images to provide ventilation-perfusion maps, which could help diagnose and locate pulmonary emboli. The lipophilicity of Xe has produced hope of imaging lipid-rich white matter in the brain, where the scarcity of free H_2O precludes conventional MRI studies, as well as investigating the properties of lipid bi-layer excitable membranes.

Our detection of a Xe NMR resonance from rat lung is a promising first step in the application of NMR-facilitated diffusion studies to the investigation of human lung microstructure. The ability to non-invasively assess the structure of the small bronchioles and alveoli would be an important advancement towards the treatment of chronic obstructive pulmonary disease (COPD), the fourth leading cause of death in the United States [2]. And because emphysema is characterized by a loss of alveolar surface area (leading to decreased aptitude for gas exchange), restricted diffusion NMR methods could quantitatively evaluate the degree of S/V loss and help identify candidates for lung volume reduction surgery (LVRS). Knowledge of local microstructure would help identify which areas of patients' lungs are the most abnormal and therefore prone to removal.

REFERENCES

- [1] <http://www.mribook.com/Purcell.htm>.
- [2] Patz, Interdisciplinary Seed Grant Application.
- [3] M.S. Albert, C-H. Tseng, D. Williamson, E.R. Oteiza, R.L. Walsworth, B. Kraft, D. Kacher, B.L. Holman, and F. Jolesz, *J. Magn. Reson. Series B* **111:2**, 204 (1996).
- [4] X.J. Chen, M.S. Chawla, L.W. Hedlund, H.E. Möller, J.R. MacFall, G.A. Johnson, *Magn. Reson. Med.* **39**, 79 (1998).
- [5] T.L. Chenevert, J.A. Brunberg, and J.G. Pipe, *Radiology* **177**, 401 (1990).
- [6] A.G. Sorensen, F.S. Buonano, G. Gonzalez, *et al.*, *Radiology* **199**, 391 (1996).
- [7] R.L. Liboff, *Introductory Quantum Mechanics* (Addison-Wesley, Reading, MA, 1992), p. 519 ff.
- [8] A. Abragam, *Principles of Nuclear Magnetism* (Oxford University Press, Oxford, 1994), p. 133 ff.
- [9] A. Kak and M. Slaney, *Principles of Computerized Tomographic Imaging* (IEEE Press, New York, 1988), p. 163.
- [10] R.J. Abraham, J. Fisher, and P. Loftus, *Introduction to NMR Spectroscopy* (John Wiley & Sons, Chichester, U.K., 1988), p. 123 ff.
- [11] R. Mair, personal communication.
- [12] H.Y. Carr and E.M. Purcell, *Phys. Rev.* **94**, 630 (1954).
- [13] M.E. Wagshul and T.E. Chupp, *Phys. Rev. A* **49**, 3854 (1994).
- [14] T.G. Walker and W. Happer, *Rev. Mod. Phys.* **69:2**, 629 (1997).
- [15] E.R. Oteiza, PhD thesis, Harvard University (1992).
- [16] T.E. Chupp, K.P. Coulter, T.B. Smith, R.C. Welsh, and M.A. Rosenberry, *Nucl. Instrum. Methods Phys. Res. Series A* **402:2-3**, 250 (1998).
- [17] E.O. Stejskal and J.E. Tanner, *J. Chem. Phys.* **42**, 288 (1965).
- [18] L.L. Latour, L. Li, and C.H. Sotak, *J. Magn. Reson.* **101**, 72-77 (1993).
- [19] J.E. Tanner and E.O. Stejskal, *J. Chem. Phys.* **49**, 1768 (1968).

- [20] J.E. Tanner, *J. Chem. Phys.* **52**, 2523 (1970).
- [21] R.M. Cotts, M.J.R. Hoch, T. Sun, and J.T. Marker, *J. Magn. Reson.* **83**, 252 (1989).
- [22] R.F. Karlicek and I.J. Lowe, *J. Magn. Reson.* **37**, 75 (1980).
- [23] G.J. Barker and T.H. Mareci, *J. Magn. Reson.* **83**, 11 (1989).
- [24] P.P. Mitra, P.N. Sen, and L.M. Schwartz, *Phys. Rev. B* **47**, 8565 (1993).
- [25] L.Z. Wang, A. Caprihan, and E. Fukushima, *J. Magn. Reson.* **117**, 209 (1995).
- [26] L.L. Latour, P.P. Mitra, R.L. Kleinberg, and C.H. Sotak, *J. Magn. Reson.* **101**, 342 (1993).
- [27] P.N. Sen, L.M. Schwartz, P.P. Mitra, and B.I. Halperin, *Phys. Rev. B* **49**, 215 (1994).
- [28] M.D. Hürlimann, K.G. Helmer, L.L. Latour, and C.H. Sotak, *J. Magn. Reson. Series A* **111**, 169 (1994).
- [29] C. Kittel and H. Kroemer, *Thermal Physics* (W.H. Freeman and Company, New York, 1995), p. 396.
- [30] R. Walsworth, personal communication.
- [31] M.S. Albert and D. Balamore, *Nucl. Instrum. Methods Phys. Res. Series A* **402**, 441 (1998).
- [32] K. Sakai, A.M. Bilek, E. Oteiza, R.L. Walsworth, D. Balamore, F.A. Jolesz, and M.S. Albert, *J. Magn. Reson., Series B* **111**, 300 (1996).
- [33] D. Hoffmann, personal communication.
- [34] G. Wong, personal communication.
- [35] X.J. Chen, M.S. Chawla, L.W. Hedlund, H.E. Möller, J.R. MacFall, G.A. Johnson, *Magn. Reson. Med.* **39**, 79 (1998).
- [36] A. Hasse, J. Frahm, D. Matthaie, W. Haenicke, and K.D. Merboldt, *J. Magn. Reson.* **67**, 258 (1986).
- [37] L.L. Latour, P.P. Mitra, R.L. Kleinberg, and C.H. Sotak, *J. Magn. Reson. Series A* **101**, 342 (1993).
- [38] R.W. Mair, D.G. Cory, S. Peled, C-H. Tseng, S. Patz, and R.L. Walsworth, submitted to *J. Magn. Reson.* (1998).
- [39] L. Zhao, R. Mulkern, C-H Tseng, D. Williamson, S. Patz, R. Kraft, R.L. Walsworth, F.A. Jolesz, and M.S. Albert, *J. Magn. Reson., Series B* **113**, 179 (1996).

- [40] B.R. Patyal, J-H. Gao, R.F. Williams, J. Roby, B. Saam, B.A. Rockwell, R.J. Thomas, D.J. Stolarski, and P.T. Fox, *J. Magn. Reson.* **126**, 58 (1997).
- [41] M. Bock, *Magn. Reson. Med.* **38**, 890 (1997).
- [42] D.M. Schmidt, J.S. George, S.I. Pentilla, A. Caprihan, and E. Fukushima, *J. Magn. Reson.* **129**, 184 (1997).
- [43] S. Peled, C-H. Tseng, A.A. Sodickson, R.W. Mair, R.L. Walsworth, and D.G. Cory, submitted to *J. Magn. Reson.* (1998).
- [44] G. Topulos, personal communication.
- [45] K.C. Hasson, G.D. Cates, K. Lerman, P. Bogorad, and W. Happer, *Phys. Rev. A* **41**, 3672 (1990).
- [46] J.O. Hirshfelder, C.F. Curtiss, and R.B. Bird, *Molecular Theory of Gases and Liquids* (Wiley, New York, 1954), p. 581.
- [47] P.N. Sen, M.D. Hürlimann, T.M. de Swiet, *Phys. Rev. B* **51**, 601 (1995).
- [48] R. Walsworth, personal communication.

ACKNOWLEDGMENTS

Writing this thesis proved to be quite a task, and there are several people whom I would like to thank for their assistance. Thanks go first to Ron Walsworth, my adviser, for his attention to my progress and learning over the course of the last year and a half. His explanations and urgings encouraged me to stick with it, and I have surely profited from the experience.

Glenn Wong was an excellent teacher, and was always there to explain things again and again until they sunk in. He quizzed me pointedly to make sure I understood what lay behind my waving hands... and he's a great skipper, too! Dominik Hoffmann was always happy to have me hanging around the polarization cart, where I learned most of what little I know about NMR. If I looked over his shoulder I was certainly the first to see the hottest new software release. I wish him happiness in married life. Sam Patz was an excellent mentor, and his constant observance that I understand the underlying physics contributed greatly to my knowledge. Thanks also to Ross Mair for taking the time to impart upon me an appreciation for the joys of diffusion and NMR.

I also want to thank Dave Bear for his willingness to sit down and explain the concepts in between musings upon the prospects of the Rockets or Lakers, the Astros or Dodgers. Ching-Hua Tseng, Rick Stoner, and Dave Phillips were also happy to answer my questions and point me in the right direction.

A hearty thanks to my thesis readers, Professors Costas Papaliolios and Bob Westervelt, who have to – get to, that is – read this endeavor of mine.

Without the support of my family I wouldn't be here in the first place, so a warm thanks goes out to them – Dad, Mom, Nuni, and Suni. And a special thanks – even though I'm not supposed to – to Sarita, who makes everything worth it.